The Astrophysical Journal, 1003:112 (19pp), 2026 June 1 https://doi.org/10.3847/1538-4357/ae5e4c

A Fleeting GLIMPSE of N/O Enrichment at Cosmic Dawn: Evidence for Wolf Rayet N Stars in a $z = 6.1$ Galaxy

Danielle A. Berg[1,2], Rohan P. Naidu[3], John Chisholm[1,2], Hakim Atek[4], Seiji Fujimoto[5], Vasily Kokorev[1,2], Lukas J. Furtak[1,2], Chiaki Kobayashi[6], Daniel Schaerer[7,8], Angela Adamo[9], Qinyue Fei[10], Damien Korber[7], Jorryt Matthee[11], Rui Marques-Chaves[7], Zorayda Martinez[1,2], Kristen. B. W. McQuinn[12,13], Julian B. Muñoz[1,2], Pascal A. Oesch[7,14], Alberto Saldana-Lopez[15], Daniel P. Stark[16], Mabel G. Stephenson[1,2], and Tiger Yu-Yang Hsiao[1,2]

[1] Department of Astronomy, The University of Texas at Austin, 2515 Speedway, Stop C1400, Austin, TX 78712, USA
[2] Cosmic Frontier Center, The University of Texas at Austin, Austin, TX 78712, USA
[3] MIT Kavli Institute for Astrophysics and Space Research, 70 Vassar Street, Cambridge, MA 02139, USA
[4] Institut d'Astrophysique de Paris, CNRS, Sorbonne Université, 98bis Boulevard Arago, 75014, Paris, France
[5] David A. Dunlap Department of Astronomy and Astrophysics, and Department of Physics, 60 Saint George Street, University of Toronto, Toronto, ON M5S 3H8, Canada
[6] Centre for Astrophysics Research, Department of Physics, Astronomy and Mathematics, University of Hertfordshire, College Lane, Hatfield AL10 9AB, UK
[7] Observatoire de Geneve, Universite de Geneve, Chemin Pegasi 51, 1290 Versoix, Switzerland
[8] CNRS, IRAP, 14 Avenue E. Belin, 31400 Toulouse, France
[9] Department of Astronomy, Oskar Klein center, Stockholm University, AlbaNova University center, SE-106 91 Stockholm, Sweden
[10] David A. Dunlap Department of Astronomy and Astrophysics, University of Toronto, 50 Saint George Street, Toronto, Ontario, M5S 3H4, Canada
[11] Institute of Science and Technology Austria (ISTA), Am Campus 1, 3400 Klosterneuburg, Austria
[12] Space Telescope Science Institute, 3700 San Martin Drive, Baltimore, MD 21218, USA
[13] Rutgers University, Department of Physics and Astronomy, 136 Frelinghuysen Road, Piscataway, NJ 08854, USA
[14] Cosmic DAWN Center, Niels Bohr Institute, University of Copenhagen, Jagtvej 128, København N, DK-2200, Denmark
[15] Department of Astronomy, Oskar Klein Centre, Stockholm University, 106 91 Stockholm, Sweden
[16] Department of Astronomy, University of California, Berkeley, Berkeley, CA 94720, USA

Received 2025 November 12; revised 2026 April 3; accepted 2026 April 11; published 2026 May 20

Abstract

We present the discovery of extreme nitrogen enrichment by Wolf Rayet nitrogen (WN) stars in the metal-poor ($\sim 10\% Z_{\odot}$), lensed, compact ($R_{\rm eff} \sim 20$ pc) galaxy RXCJ2248 at $z = 6.1$, revealed by unprecedentedly deep JWST/NIRSpec medium-resolution spectroscopy from the GLIMPSE-D Survey. The exquisite signal-to-noise ratio reveals multiple high-ionization nebular lines and broad Balmer and [O III] components (FWHM $\sim$700–3000 km s^{-1}). We detect broadened He II λ1640 and λ4687 (FWHM $\sim$ 530 km s^{-1}) and strong N III λ4642 emission consistent with a population of WN stars, making RXCJ2248 the most distant galaxy with confirmed Wolf Rayet (WR) features to date. We measure the multiphase nebular density across five ions, the direct-method metallicity (12 + log(O/H) = 7.753 ± 0.025), and a nonuniform elemental enrichment pattern of extreme N/O enhancement (log(N/O) = −0.391 ± 0.037 from N^{+}, N^{+2}, and N^{+3}) but suppressed C/O relative to empirical C/N trends. We show that this abundance pattern can be explained by enrichment from a dual-burst with a low WR carbon/WN ratio, as expected at low metallicities. Crucially, these signatures can only arise during a brief, rare evolutionary window shortly after a burst ($\sim$3–6 Myr), when WN stars dominate chemical feedback but before dilution by later yields (e.g., supernovae). The observed frequency of strong N emitters at high$-z$ implies a $\sim$50 Myr burst duty cycle, suggesting that N/O outliers may represent a brief but ubiquitous phase in the evolution of highly star-forming early galaxies. The WN detection in RXCJ2248, therefore, provides the first direct evidence of WR-driven nitrogen enrichment in the first billion years of the Universe and a novel timing argument for the bursty star formation cycles that shaped galaxies at cosmic dawn.

Unified Astronomy Thesaurus concepts: Chemical abundances (224); Chemical enrichment (225); H II regions (694); Interstellar medium (847); Interstellar line emission (844); High-redshift galaxies (734); Star forming regions (1565); Galaxy chemical evolution (580); Wolf-Rayet stars (1806)

1. Introduction

A key tracer of galaxy evolution is the change in their chemical composition over time. The metallicity of a galaxy is a sensitive observational diagnostic of its past star formation history and present-day evolutionary state given that metallicity increases with each successive generation of massive star yields (e.g., M. Tosi 1988; J.-R. Roy & D. Kunth 1995; D. A. Berg et al. 2019; R. Maiolino & F. Mannucci 2019). Oxygen is an important tracer of metallicity because it is the most abundant element in the Universe after H and He and is convenient to observe, with ubiquitous emission lines from H II regions in the rest-frame optical regime. While O emission in dwarf and spiral galaxies has been widely observed in the rest-frame optical and UV (e.g., R. C. Kennicutt 1992; Y. I. Izotov & T. X. Thuan 1999; L. van Zee & M. Haynes 2006; D. A. Berg et al. 2012, 2016, 2019; P. Senchyna et al. 2017; N. S. J. Rogers et al. 2022), the N emission in these same galaxies has been predominantly traced only in the optical through the low-ionization [N II] $\lambda\lambda$6550,6585 emission lines. In general, there is a surprising dearth of detections of the high-ionization N emission counterparts in local galaxies, totaling less than 10 galaxies with significant detections of either N IV] $\lambda\lambda$1483,1486 or N III] λ1750 (e.g., M. Mingozzi et al. 2022; Z. Martinez et al. 2025). However, with the advent of JWST, there is a growing prevalence of $z \gtrsim 5$ galaxies with extreme properties, including intense UV N emission (e.g., A. J. Bunker et al. 2023; Y. Isobe et al. 2023; M. Castellano et al. 2024; T. Y.-Y. Hsiao et al. 2024; X. Ji et al. 2024; R. Marques-Chaves et al. 2024; D. Schaerer et al. 2024; M. Curti et al. 2025a; Y. Harikane et al. 2025a; R. P. Naidu et al. 2026; M. W. Topping et al. 2025b).

The first noted, and one of the most distant, examples of extreme rest-frame UV N emission comes from the spectroscopically confirmed $z = 10.6$ galaxy, GN-z11. JWST spectra of GN-z11 revealed surprisingly strong N IV] $\lambda\lambda$1483,1486 and N III] λ1750 emission (e.g., A. J. Bunker et al. 2023) that corresponds to supersolar nitrogen-to-oxygen (N/O) enrichment ($\log(\mathrm{N/O}) > -0.25$; e.g., A. J. Cameron et al. 2023). Subsequently, enhanced N/O has been reported in a number of high$-z$ galaxies, including GDS 3073 ($z = 5.55$; X. Ji et al. 2024), RXCJ2248-ID ($z = 6.10$; M. W. Topping et al. 2024), A1703-zd6 ($z = 7.04$; M. W. Topping et al. 2025b), CEERS-1019 ($z = 8.68$; R. Marques-Chaves et al. 2024), GNz9p4 ($z = 9.38$; D. Schaerer et al. 2024), GHZ9 ($z = 10.15$; L. Napolitano et al. 2025), GHZ2 ($z = 12.34$; M. Castellano et al. 2024), and MoM-z14 ($z = 14.44$; R. P. Naidu et al. 2026). For a review of nitrogen line detections, see D. P. Stark et al. (2025). Such strong nebular N^{+3} emission requires a relatively hard ionizing radiation field ($\gtrsim$47.4 eV), where models of massive stars predict few photons. On the other hand, N^{+2} has a lower ionization potential ($\sim$29.6 eV), but statistically significant detections are strikingly rare in integrated galaxy spectra (e.g., D. A. Berg et al. 2018; M. Mingozzi et al. 2022; A. J. Bunker et al. 2023; P. Senchyna et al. 2024) and are only expected to be strong at the highest possible nebular temperatures ($\sim 2.5 \times 10^4$ K). Furthermore, the timing of the incredibly high N/O abundances reported for the high-redshift UV N emitters just a few 100 Myr after the Big Bang is unexpected.

The discovery of significant, rapid nitrogen enhancement so early in the Universe was surprising because it contradicts our longstanding understanding of N production. In typical chemical evolution modeling, some nitrogen enrichment can occur early on via core collapse supernova (CCSN), but substantial nitrogen enrichment only occurs 100 s of megayears after the onset of star formation via asymptotic giant branch (AGB) stars (e.g., F. Vincenzo et al. 2019; C. Kobayashi et al. 2020). Thus, alternative, faster enrichment methods are needed to explain substantial nitrogen enrichment in early galaxies. As a result, the necessary ionizing flux and conditions to produce the unexpectedly strong N^{+3} and N^{+2} emission observed in galaxies beyond $z \sim 5$ have been attributed to more extreme sources, such as active galactic nuclei (AGN; R. Maiolino et al. 2024), Wolf Rayet (WR) stars (e.g., P. Senchyna et al. 2024; K. Watanabe et al. 2024; M. L. P. Gunawardhana et al. 2025), globular cluster precursors (e.g., C. Charbonnel et al. 2023; X. Ji et al. 2026), super star clusters (e.g., M. Pascale et al. 2023), very massive stars (VMSs: $M_\star > 10^2\,M_\odot$; e.g., J. S. Vink 2023; Y. Shi et al. 2026), or supermassive stars ($M_\star > 10^3\,M_\odot$; e.g., C. Charbonnel et al. 2023; C. Nagele & H. Umeda 2023), tidal disruption events (e.g., A. J. Cameron et al. 2023; K. Watanabe et al. 2024), and more.

Most of our understanding of WR stars has been built from observations of individual resolved stars in a handful of galaxies in the Local Group, with almost no direct spectroscopic evidence for the prevalence of WR stars in more distant galaxies. To date, only two systems at Cosmic Noon ($z \approx 2$–3) have confirmed signatures of WR stars: MARTA-4327 at $z = 2.224$ (hereafter, M4327; M. Curti et al. 2025b) and the Sunburst Arc at $z = 2.37$ (T. E. Rivera-Thorsen et al. 2024). Extending such detections to earlier cosmic epochs is crucial for understanding the role of massive stars in shaping the chemical evolution of galaxies in the first Gyr.

Here, we investigate the $z = 6.1$ lensed galaxy RXCJ2248-ID3. RXCJ2248-ID was first identified by F. Boone et al. (2013), I. Balestra et al. (2013), and A. Monna et al. (2014) and discovered to be a high-ionization, compact, metal-poor, N-enhanced galaxy by R. Mainali et al. (2017), K. B. Schmidt et al. (2017), and M. W. Topping et al. (2024). We present extremely deep JWST/NIRSpec observations of RXCJ2248-ID3 that provide the highest-redshift spectroscopic evidence of WR nitrogen (WN) stars to date, which provide a physically consistent mechanism driving its extreme nitrogen enrichment (M. W. Topping et al. 2024). The remainder of this paper is organized as follows. The observations and data reduction are briefly described in Section 2.1, followed by a description of the emission-line fits, including the broad lines related to the WR feedback, in Section 2.2. We present the discovery of WN stars at $z \sim 6$ via their spectral signatures in Section 3. We determine new nebular properties and O, C, N, and Si abundances in Section 4.3 and compare them to populations of both low- and high-redshift galaxies. We discuss the source of N enrichment in the early Universe and subsequently estimate mass production and timing arguments in Section 5. Finally, we present our conclusions in Section 6. Throughout this work, we adopt cosmological parameters of $H_0 = 70\ \mathrm{km\,s^{-1}\,Mpc^{-1}}$, $\Omega_\mathrm{m} = 0.30$, and $\Omega_\Lambda = 0.7$ and the solar abundance pattern from M. Asplund et al. (2021).

2. JWST/NIRSpec Spectra

RXCJ2248 is a galaxy at $z \sim 6.1$ that is lensed into multiple images by the Abell S1063 cluster (α = 22:48:44.13, δ = −44:31:57.50) at a redshift of $z = 0.348$. We present an analysis of the brightest image, RXCJ2248-ID3 ($J = 25.0$), which has a magnification of $\mu \sim 7$ (L. Furtak et al. 2025). RXCJ2248-ID was discovered as a $z \sim 6$ candidate (F. Boone et al. 2013; A. Monna et al. 2014) using the 16-band HST photometry of the CLASH Survey and spectroscopically confirmed via VIsible Multi-Object Spectrograph (VIMOS)/VLT observations by I. Balestra et al. (2013). RXCJ2248-ID3 was soon found to be an exciting extreme emission-line galaxy via ground-based spectroscopy (R. Mainali et al. 2017), with strong detections of high-ionization emission such as O III] $\lambda\lambda$1661,1666 and C IV $\lambda\lambda$1548,1550 but no He II, suggesting star formation as the ionizing source rather than an AGN.

The early spectra of RXCJ2248-ID3 motivated further rest-UV+optical study with JWST/NIRSpec by M. W. Topping et al. (2024). This work performed direct metallicity calculations to show that RXCJ2248-ID3 is one of the most extreme N/O-enhanced ($\log(\mathrm{N/O}) = -0.39^{+0.11}_{-0.10}$), metal-poor ($12 + \log(\mathrm{O/H}) = 7.43^{+0.17}_{-0.09}$) galaxies, with high-ionization ([O III] λ5008/[O II] λ3728 = 184) and high nebular density

Table 1
Properties of RXCJ2248-ID3

JWST/NIRSpec Observations		
Grating/Filter	$t_{\rm exp}$ (s)	PI/PID
G140M/F100LP	6215	Stark/2478
G235M/F170LP	1576	Stark/2478
G395M/F290LP	107,228	Fujimoto & Naidu/9223
Measured Properties		
Property	Value	References
R.A.	+22:48:45.81	This work
Decl.	−44:32:14.95	This work
z	6.1025 ± 0.0013	This work
μ	6.8877	L. Furtak et al. (2025)
$R_{\rm eff}$ (pc)	$19.5^{+13.99}_{-4.72}$	A. Claeyssens (2025)
$M_\star$ ($M_\odot$)	$4.6^{+21.1}_{-2.3} \times 10^7$	A. Claeyssens (2025)
$\Sigma_\star$ ($M_\odot$ pc^{-2})	$1.1^{+5.2}_{-0.3} \times 10^4$	A. Claeyssens (2025)
SFR$_{\rm H\alpha}$ ($M_\odot$ yr^{-1})	3.2	This work, Section 5.3
SFR$_{\rm SED,1Myr}$ ($M_\odot$ yr^{-1})	4.7	A. Claeyssens (2025)
SFR$_{\rm SED,10Myr}$ ($M_\odot$ yr^{-1})	4.1	A. Claeyssens (2025)
$\Sigma_{\rm SFR}$ ($M_\odot$ yr^{-1} kpc^{-2})	1.34×10^3	This work
$t_{\rm age}$ (Myr)	$1.6^{+11.9}_{-0.9}$	A. Claeyssens (2025)
12+log(O/H)	7.753 ± 0.025	This work, Section 4.3.1
log(N/O)	−0.391 ± 0.037	This work, Section 4.3.2

Note. Top: JWST/NIRSpec observations of RXCJ2248-ID3, including archival observations from PID 2478 (PI: Stark) and very deep GLIMPSE-D observations from PID 9223 (PI: Fujimoto & Naidu). Columns (1)–(3) list the grating/filter, exposure time, and principle investigator/PID. Bottom: Measured global properties of RXCJ2248-ID3. The R.A. and decl. are the extraction coordinates for RXCJ2248-ID3. The redshift was determined from the GLIMPSE-D spectrum emission lines. GLIMPSE imaging was used to determine the lensing model magnification, μ. Effective radius of the RXCJ2248-ID3 clump, stellar mass, and current massive star population age are from the SED modeling of A. Claeyssens (2025), while the SFR was determined from both the SED fitting and the narrow-component, collisions-corrected Hα flux (see Section 5.3), all corrected for the lensing factor. The star formation rate surface density was determined using the SFR$_{\rm H\alpha}$. The metallicity and relative N/O abundance were determined using the direct method.

($6.4 \times 10^4 \leqslant n_e({\rm cm}^{-3}) \leqslant 3.1 \times 10^5$). They also used spectral energy distribution (SED) fitting with a constant star formation history to characterize its low stellar mass ($M_\star \sim 10^8\,M_\odot$) and the young-massive star population (∼2 Myr) of RXCJ2248. M. W. Topping et al. (2024), therefore, suggest that the N/O enrichment may be due to a short-lived phase that many $z > 6$ bursty galaxies experience. In this paper, we build on the work of M. W. Topping et al. (2024) with new, extraordinarily deep rest-optical JWST/NIRSpec observations of RXCJ2248-ID3 from the GLIMPSE-D Survey, a Director's Discretionary Time (DDT) follow-up program described below.

2.1. Observations and Reduction

The work presented here uses both the rest-UV JWST/NIRSpec archival spectra from JWST PID 2478 (PI Stark) and new rest-optical JWST/NIRSpec spectra from the GLIMPSE-D Survey, which is an extension of the GLIMPSE Survey. Properties of RXCJ2248-ID and observation details are presented in Table 1.

The GLIMPSE Survey is a large Cycle 2 JWST program (PID 3293; PIs Atek & Chisholm) that performed ultradeep NIRCam imaging (∼30.8 mag at 5σ over 0.8–5 μm) in seven broadband and two medium-band filters of the lensing cluster Abell S1063 (H. Atek et al. 2025). A. Claeyssens (2025) performed size and photometric measurements of RXCJ2248-ID in the different multiple images. The SED fitting was performed with the Bayesian Analysis of Galaxies for Physical Inference and Parameter Estimation (`BAGPIPES`; A. C. Carnall et al. 2018) code with Binary Population and Spectral Synthesis (`BPASS` v2.14, J. J. Eldridge et al. 2017) stellar population synthesis burst models and `cloudy` v23.01 photoionization models (M. Chatzikos et al. 2023; C. M. Gunasekera et al. 2023). Priors were used to be physically consistent with the source, i.e., high-ionization parameter ($-2 \leqslant \log U \leqslant -1$), low extinction ($A_v < 0.5$ mag), low metallicity ($Z < 0.4\,Z_\odot$), and bursty star formation ($\tau = 1$ Myr, i.e., close to a single burst, or $\tau = 10$ Myr). The resulting best fit has a young age ($t_{\rm age} = 1.6^{+11.9}_{-0.9}$ Myr) and low stellar mass of $M_\star = 4.6^{+21.1}_{-2.3} \times 10^7\,M_\odot$ but within a compact size of $R_{\rm eff} = 19.5^{+13.99}_{-4.72}$ pc such that the stellar mass surface density is $\Sigma_\star = 1.1^{+5.2}_{-0.3} \times 10^4\,M_\odot$ pc^{-2}. This value is akin to the highest densities found in globular clusters, similar to the ones reported for young star clusters and clumps at high redshift (A. Claeyssens et al. 2025; M. Messa et al. 2026), and broadly consistent with the conclusions presented in M. W. Topping et al. (2024).

Subsequent medium-resolution ($R \sim 1000$) spectra of RXCJ2248-ID3 were obtained as part of the follow-up GLIMPSE-D Survey: JWST DDT Program 9223 (PIs Fujimoto & Naidu) targeting a Pop III candidate in S. Fujimoto et al. (2025) using NIRSpec Multi-Object Spectroscopy (MOS) with the G395M grating and F290LP filter. As part of this program, RXCJ2248-ID3 was observed for a total of 13 exposures using a 3-point nod pattern and NRSIRS2 readout, totaling ∼30 hr of integration. The MSA slit positions covering RXCJ2248-ID3 of the three pointings are shown in Figure 1.

We augment the rest-optical GLIMPSE-D data with archival rest-far-UV G140M/F100LP and rest-near-UV G235M/F170LP observations from PID 2478 (PI Stark), covering the rest-frame ∼1400–4000 Å range. This program also observed the G395M/F290LP setting, but we only use the significantly deeper GLIMPSE-D G395M observations here. Multiple images of RXCJ2248 were identified and observed in program #2478. M. W. Topping et al. (2024) utilized these data by coadding the spectra of the individual images. In contrast, only the brightest image (ID3) was observed in the GLIMPSE-D Survey. To ensure consistency, we therefore restricted our analysis to the G140M and G235M spectra of ID3 obtained in program #2478. As a result, our G140M and G235M measurements are not directly comparable to those presented by M. W. Topping et al. (2024).

The data were reduced using v0.9.8 of the `msaexp` pipeline (G. Brammer 2022), following the standard routines described in A. de Graaff et al. (2025), K. E. Heintz et al. (2025), and F. Valentino et al. (2025). Briefly, level-2 calibrated products from MAST are subject to a series of custom corrections that account for, e.g., 1/f noise, bar vignetting, and detector bias. We used the "local" nodded background subtraction. The 2D spectra were drizzled onto a common wavelength grid and 1D spectra were optimally extracted using a profile model that accounts for, e.g., the wavelength-dependent PSF and offsets from the nominal position expected from the catalog. Line centers were measured for the strongest emission lines in the

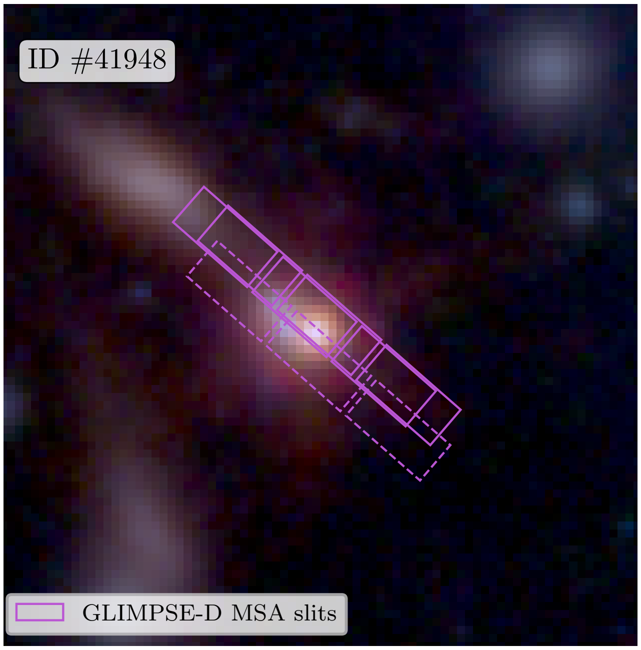

Figure 1. JWST/NIRSpec MSA slits targeting RXCJ2248-ID3 for each of the three exposures in the GLIMPSE-D program. The two pointings that are closely aligned (solid purple regions) have the same wavelength coverage, while the pointing offset to the lower left (dashed region) has somewhat reduced blue coverage. All three pointings were used in the spectrum coaddition.

G395M spectrum (i.e., Hδ, Hγ, [O III] λ4364, Hβ, [O III] $\lambda\lambda$4960,5008, He Iλ5877, Hα, He Iλ7067) and used to determine a redshift of $z = 6.1025 \pm 0.0013$. Note that the bluest portion of the G395M tends to favor a slightly lower redshift (i.e., $z \sim 6.1000$), while the reddest portion favors a slightly higher redshift (i.e., $z \sim 6.1034$). The three individual 1D extracted spectra were then normalized to the common continuum flux scale of the first spectrum at rest-wavelengths of ~6000–62000 Å prior to coadding. Spectral coaddition was performed as a weighted average using the inverse variance as the weight.

The resulting spectrum, shown in Figure 2, covers an observed wavelength range ~2.8–5.5 μm, which corresponds to a rest-optical range of ~3900–7740 Å. Note that the third pointing (dashed slits in Figure 1) has reduced wavelength coverage such that the blue end begins at ~4265. The deep GLIMPSE-D spectra provide unparalleled signal-to-noise ratio (S/N; >5 at 5100 Å continuum) that enable rest-optical diagnostics typically reserved for nearby galaxies.

2.2. Emission-line Measurements

In order to perform a consistent analysis of our data, we measure emission-line fluxes for both the archival spectra and the new GLIMPSE-D spectra presented here. We fit neighboring emission lines simultaneously using Gaussian profiles with the `lmfit` package (M. Newville et al. 2015) in `Python`. Purely nebular lines (i.e., lines without possible stellar contributions or resonant effects) close in wavelengths were constrained to have the same full width at half-maximum (FWHM) velocity widths. Additionally, the relative wavelength spacing between lines was constrained to laboratory values and doublets with constant flux ratios set by atomic physics were constrained to their theoretical values, with small uncertainty allowances. The uncertainties on the line fluxes were estimated as the standard error derived from the least-squares minimization in `lmfit`, which considers the uncertainty on the Gaussian profile and linear continuum.

Broad emission components are clearly visible at the base of some of the emission lines in the GLIMPSE-D spectrum of RXCJ2248-ID3. Such broad emission features can be produced by stellar winds, shocks, or turbulence. Since He IIλ1640 and λ4687 emission lines can be affected by stellar winds, we fit these features with an unconstrained Gaussian width. Using the `jwst-msa` package (A. de Graaff et al. 2024), we deconvolved all measured FWHMs with the modeled wavelength-dependent line spread function (LSF). We found the He II lines to be broadened compared to purely nebular lines. For the He IIλ 4687 line, the velocity width is 528 ± 100 km s^{-1}, which is more than two times broader than the narrow nebular Hβ component with $v_{\rm FWHM} = 243 \pm 25$ km s^{-1}.

The strongest rest-optical H (Hγ, Hβ, and Hα) and [O III] (λ4364, $\lambda\lambda$4960,5008) emission lines have complex profiles with both narrow and broad emission components. Such broad components may also be present in the rest-UV and fainter rest-optical emission lines, but none are obvious given the lower S/N of these emission features and/or underlying continuum. To fit these profiles, we tested three different multicomponent profile combination fits for the Hα + [N II] complex. For all three fits, the narrow Hα and [N II] $\lambda\lambda$6550,6585 lines were fit by Gaussians with a single velocity width, but the broad component was fit with either: (1) a single Gaussian profile, (2) two Gaussian profiles, or (3) a single exponential profile. The single broad Gaussian profile fit had strong residuals near the center of the broad component, so did not provide a good fit to the observed emission profile. Both the double Gaussian profile and the exponential profile provided relatively good visual fits, but the double Gaussian fit had a lower reduced chi-squared ($\chi^2_{\rm 2Gauss} = 0.93$ vs $\chi^2_{\rm exp.} = 1.52$) and Bayesian inference criteria (BIC$_{\rm 2Gauss}$ = 36 versus (BIC$_{\rm exp.}$ = 87), and so was adopted as the better statistical fit.

The right panel of Figure 3 shows the best multicomponent fit to the Hα + [N II] complex. Since all kinematically similar lines in the Balmer emission series arise from the same gas, we expect the Hβ and Hγ profiles to be well fit by scaling the Hα best fit. Therefore, we constrained the velocity widths of the Hβ and Hγ emission components to match the narrow + double broad Gaussian Hα fit, accounting for the wavelength-dependent LSF. We found excellent fit results, with similarly small reduced-χ^2 and BIC values. This means that the H I lines are well fit by a profile with (1) a strong, narrow (~250 km s^{-1}) nebular component, (2) a moderate (~20% of total flux), broad component (~670 km s^{-1}), and (3) a weak (~10% of total flux), very broad (~2530 km s^{-1}) component.

The [O III] $\lambda\lambda$4960,5008 doublet lines are also well fit by a narrow Gaussian plus double Gaussian broad component profile, with the relative fluxes of each component constrained to the theoretical ratio. While the narrow-component FWHM was set to the velocity width of the narrow Balmer lines, convolved with the LSF, we allowed the FWHM of the two broad [O III] components to vary freely and found widths of ~890 km s^{-1} and ~2980 km s^{-1}, respectively. The similarity between the [O III] and H I velocity widths of the broad components argues against emission from an AGN directly (where high densities cause collisional de-excitation of [O III]) and is more consistent with stellar or AGN driven winds (e.g.,

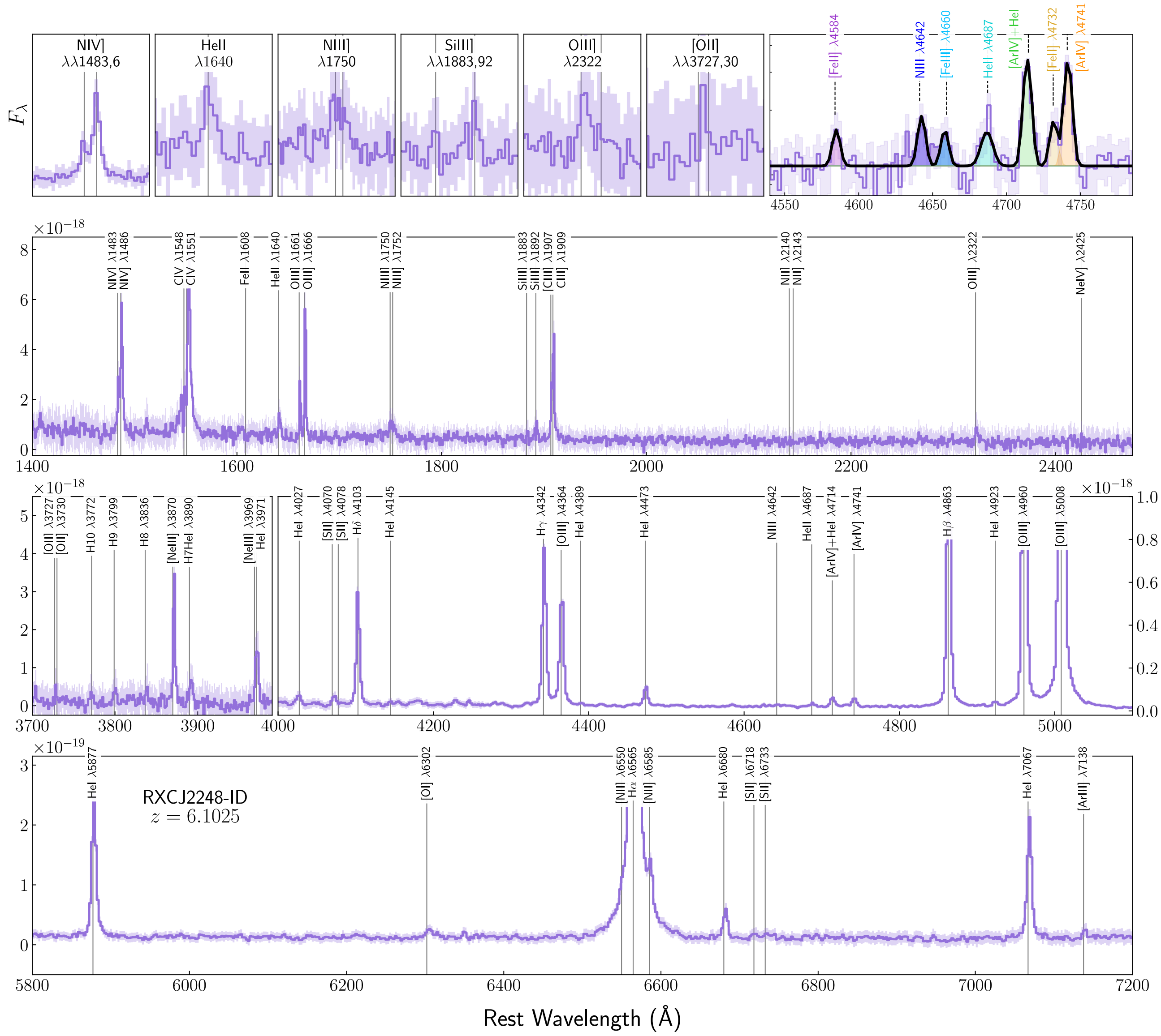

Figure 2. JWST/NIRSpec rest-frame UV and optical spectra of RXCJ2248-ID3 highlighting the first object known with simultaneously detected emission from N^{+}, N^{+2}, and N^{+3} (see, also, M. W. Topping et al. 2024) and WR features. The second row shows the main emission UV emission-line detections from the archival G140M/F100LP spectrum, with significant detections of several high-ionization emission lines, including N IV] λλ1483,1486, C IV λλ1548,1550, He II λ1640, O III] λλ1661,1666, N III] λ1750, and C III] λλ1907,1909. The third row shows the blue end of the optical spectrum, where the left-hand panel shows the archival G235M/F170LP spectrum, which includes the low-ionization [O II] λλ3727,3730 doublet. The right-hand panel of the third row and the fourth row shows the extremely high S/N GLIMPSE-D optical spectrum, enabling detections of several weak features. Note that some of the important features to this work are highlighted in the zoom in panels in the top row. In particular, the last panel reveals the most distant WR detection to date, with the λ4650 WR bump showing emission from N III λ4642, indicative of nitrogen enrichment from WN stars. Note that not all of the labeled lines correspond to line detections.

Y. I. Izotov & T. X. Thuan 2008; G. Gräfener & J. S. Vink 2015; G. Gräfener et al. 2017; C. J. Burke et al. 2021). Interestingly, the broad components of the H I lines compose a larger fraction of their total flux (∼20% and 10%, respectively) than [O III] (∼10% and 5%, respectively).

The resulting fit to the Hβ + [O III] λλ4960,5008 complex is shown in the middle panel of Figure 3 to be an excellent fit, with minimal residuals. The exquisite S/N of the GLIMPSE spectrum also reveals broad wings on the [O III] λ4364 profile, as seen in the left panel of Figure 3. Therefore, we also applied the narrow Gaussian plus double Gaussian broad component profile to [O III] λ4364, constraining the velocity widths to the values measured for [O III] λλ4960,5008.

Double broad components with similar velocity widths (750 and 2500 km s^{-1}, respectively) are seen in the $z \sim 0$ extreme emission-line galaxies, J1044+0353 and J1418+2102, reported in D. A. Berg et al. (2021). However, each broad component observed in these nearby analogs only accounts for 1%–3% of the total H I flux. This sort of broad component emission from the Balmer H and [O III] lines with widths (1000–2000 km s^{-1}) and fractional fluxes of 1%–2% is commonly found in spectra of blue compact dwarf galaxies (BCDs; e.g., Y. I. Izotov et al. 2006, 2007). This suggests that bulk motion of the gas is typical in these metal-poor, bursty environments, but for a larger mass of gas in RXCJ2248-ID3.

The sensitive accounting of broad component emission afforded by the deep GLIMPSE-D spectra is important because even a small fraction of broad emission around H emission line can significantly affect the fit to weak lines such as [N II] λλ6550,6585 (e.g., D. A. Berg et al. 2021). In

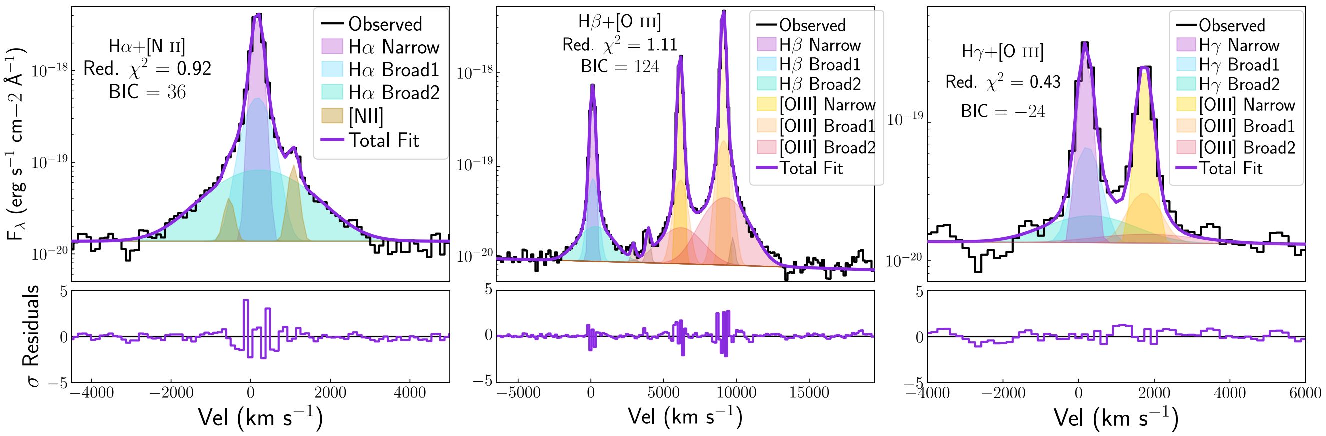

Figure 3. Multicomponent emission-line fits to the GLIMPSE spectrum of RXCJ2248-ID for Hα λ6565 + [N II] λλ6549,6585 (left panels), Hβ λ4863 + [O III] λλ4960,5008 (middle panels), and Hγ λ4342 + [O III] λ4364 (right panels). When fit with single, narrow Gaussian components (e.g., purple and yellow filled Gaussians), all three line complexes show strong, broad component residual flux. The resulting best fit to each line is comprised of a single narrow Gaussian plus two broad Gaussians, where the relevant component velocity widths are tied together: The Hα λ6565 + [N II] λλ6549,6585 complex fit provided the velocity width constraints for the H Balmer line narrow (purple Gaussians) and broad components (blue and green Gaussians) and, subsequently, the Hβ λ4863 + [O III] λλ4960,5008 fit constrained the [O III] narrow (yellow Gaussian) and broad (orange and red Gaussians) velocity widths that were then used in the Hγ λ4342 + [O III] λ4364 fit. Note that additional faint lines (e.g., He I λ5017) were included in the fit in the middle panel. Careful accounting for the residual broad flux has a significant impact on the derived nebular reddening, temperature, metallicity, and N/O abundance.

RXCJ2248-ID, the broad components compose a significant fraction of the total H and [O III] fluxes, and so are critical to properly measure not only the [N II] λ6585 emission but also the [O III] λ4364, Hβ, [O III] λλ4960,5008, and Hα narrow-line fluxes. For this reason, we adopt the narrow-line fluxes from our best multicomponent fits for the remaining analysis; we reserve further investigation of the the broad emission for a forthcoming paper.

As noted above, the UV spectra do not have sufficient S/N to decompose narrow and possible broad components. As a result, density diagnostics and relative abundance ratios determined from UV line ratios may include contributions from multiple kinematic components. If the broad components arise from gas with distinct physical conditions, this could introduce systematic offsets. We test the level of bias possible due to broad component contamination of narrow-line fluxes by adopting the relative narrow and broad component profiles of [O III] λ5008 as a template for collisionally excited lines. The broad component areas overlap with the narrow profile such that the broad components are responsible for 8.6% and 2.2% of the narrow-component flux, or 10.8% in total. We use this fraction to set the upper contamination limit of potential broad components to the UV emission lines and determine the impact on nebular density, temperature, and abundance calculations in Section 4.4.

2.3. Reddening Correction

The observed Balmer decrement of the narrow Hα/Hβ lines is $F_{\mathrm{H}\alpha}/F_{\mathrm{H}\beta} = 3.48$, implying either a moderate amount of dust is present or collisional enhancement of Hα. This value disagrees with the results of M. W. Topping et al. (2024), who measured an observed decrement of 2.55 ± 0.05 that they found to be consistent with no dust attenuation. Similarly, A. Crespo Gómez et al. (2025) used high-resolution NIRSpec/G395H data to fit multiple component Balmer decrements for RXCJ2248-ID3, finding a narrow-component $F_{\mathrm{H}\alpha}/F_{\mathrm{H}\beta} = 2.7$ that is consistent with no attenuation, but broad- and very broad-component decrements of 4.3 and 6.6, respectively, that imply differential extinction. We too find higher $F_{\mathrm{H}\alpha}/F_{\mathrm{H}\beta}$ ratios for the broad components, but the source of this increase is not clear; it could indicate higher dust in the broad component gas, as suggested by A. Crespo Gómez et al. (2025), or result from significant collisional enhancement of Hα.

Fortunately, the GLIMPSE-D spectrum provides a significant increase in S/N in the continuum, allowing for more robust fitting of broad components, including in the Hγ and [O III] λ4364 and λ5008 lines. Fitting the broad components directly in the [O III] lines offers the advantage over previous works that we do not need to correct for broad component contamination with differential extinction in our T_e calculation. Furthermore, by fitting the broad components in Hγ we were able to examine the narrow-component Hβ/Hγ ratio, finding a decrement of $F_{\mathrm{H}\beta}/F_{\mathrm{H}\gamma} = 2.16$ that is consistent with very little dust (see Table 2). Note that we do not consider the Hβ/Hδ ratio here because the Hδ line is not strong enough to robustly fit the broad components in a consistent manner with the profile fitting of the Hγ, Hβ, and Hα lines.

The reddening due to dust, characterized by $E(B-V)$, was determined by comparing the observed Balmer decrements with the theoretical Balmer ratios assuming case B and an extinction law, for which we tested the parameterization from both J. A. Cardelli et al. (1989) and D. Calzetti et al. (2000). The $E(B-V)$ value for a given Balmer ratio was determined iteratively until convergence, recomputing the H I theoretical ratio using the updated electron temperature from the reddening-corrected [O III] λ4364/λ5008 flux ratio and density from the reddening-corrected N IV] λ1483/λ1487 flux ratio in each iteration. In this way, the reddening, electron temperature, and electron density were solved for simultaneously and consistently.

A greater enhancement of the observed $F_{\mathrm{H}\alpha}/F_{\mathrm{H}\beta}$ decrement than of the $F_{\mathrm{H}\beta}/F_{\mathrm{H}\gamma}$ decrement can arise under high-density conditions, where collisional excitation selectively enhances the lowest excited level ($n = 2$; requires lowest energy to excite), leading to higher Hα flux relative to Hβ and Hγ. To assess whether such an enhancement is physically plausible, we examined the `Cloudy` photoionization models

Table 2
Rest UV+Optical Emission-Line Fluxes

Ion+Wavelength (Å)	$I(\lambda)/I$(C III])	EW (Å)
N IV] λ1483.33	42.78 ± 1.61	6.67
N IV] λ1486.50	102.0 ± 0.82	15.9
He IIλ1640.42	22.46 ± 197	4.88
O III] λ1666.15	85.84 ± 0.59	18.9
N III] λ1750[a]	38.59 ± 0.64	9.18
Si III] λ1883.00	5.01 ± 3.25	1.32
Si III] λ1892.03	8.25 ± 1.98	2.21
C III] λ1906.68	35.11 ± 0.31	9.65
[C III] λ1908.73	64.89 ± 0.25	17.9
Ion+Wavelength (Å)	$I(\lambda)/I(\mathrm{H}\beta)$	EW (Å)
[O II] λ3728[a]	4.09 ± 2.05	6.22
Hγ λ4341.66[b]	47.41 ± 3.07	73.8
[O III] λ4364.44[b]	42.45 ± 1.92	66.5
He I λ4472.73	8.90 ± 0.39	27.8
N III λ4641.94	1.40 ± 0.20	4.4
He II λ4687.01	1.33 ± 0.29	4.2
[Ar IV] λ4712.69[c]	2.30 ± 0.27	10.3
He I λ4714.46[c]	1.91 ± 0.19	3.0
[Ar IV] λ4741.49	4.10 ± 0.26	13.0
Hβ λ4862.71[b]	100.0 ± 4.4	356
[O III] λ4960.29[b]	230.5 ± 9.0	877
[O III] λ5008.24[b]	708.9 ± 27.5	2791
Hα λ6564.60[b,d]	331.8 ± 14.4	1755
Hα λ6564.60[b,e]	274.1 ± 11.9	1457
[N II] λ6585.27	7.08 ± 0.91	12.8
[S II] λ6718.29	0.68 ± 0.29	4.78
[S II] λ6732.67	0.81 ± 0.30	4.74
$E(B-V)$	$0.052^{+0.110}_{-0.052}$	⋯
$F_{\mathrm{C\,III]}}$	11.58 ± 0.49	⋯
$F_{\mathrm{H}\beta}$[b]	6.94 ± 0.15	⋯

Notes. Reddening-corrected emission-line intensities of lines used in this analysis from the archival rest-UV and GLIMPSE rest-optical JWST/NIRSpec spectra for RXCJ2248-ID3. Note that no scaling was performed between the archival UV and GLIMPSE-D optical pointings (not needed for this work). Thus, UV fluxes are given relative to the $F_{\mathrm{C\,III]}\lambda\lambda1907,09} \times 100$ and optical fluxes are given relative to $F_{\mathrm{H}\beta} \times 100$. The last three rows list the dust attenuation derived using the J. A. Cardelli et al. (1989) reddening law and the rest-frame C III] $\lambda\lambda$1907,09 and Hβ flux in units of 10^{-18} erg s^{-1} cm^{-2}. Additionally, the fluxes reported here are for a single image of RXCJ2248 (ID3), whereas M. W. Topping et al. (2024) report fluxes for coadded spectra of multiple images.

[a] Note that N III] λ1750 and [O II] λ3728 fluxes are the integrated values for the N III] $\lambda\lambda$1746,1748,1749,1752,1754 quintuplet and [O II] $\lambda\lambda$3727,3730 doublet, respectively.

[b] Emission-line profile was best fitted with a narrow Gaussian and two broad Gaussian components; only the corrected narrow-line flux is listed here (see Section 2.2 and Figure 3).

[c] [Ar IV] λ4713+He Iλ4714 is a blended line profile at the observed resolution. Thus, the [Ar IV] λ4713 is determined by subtracting the He Iλ4714 flux, which is predicted from the He I λ4473 flux.

[d] Uncorrected for collisional excitation.

[e] Corrected for collisional excitation.

(M. Chatzikos et al. 2023; C. M. Gunasekera et al. 2023) presented in Z. Martinez et al. (2025), which span a wide range of nebular densities (up to $n_e = 10^9$ cm^{-3}). For the nebular conditions determined in this work (i.e., T_e, log U, Z, N/O; see Section 4), densities of $n_e \sim 10^6$ cm^{-3} are needed to produce the observed Hα enhancement while minimally affecting Hβ and Hγ. Although this density is roughly an order of magnitude higher than the values measured in M. W. Topping et al. (2024) and in this study (see Section 4.1 and Table 3), it could indicate that the interstellar medium (ISM) contains unresolved clumps of even higher density than the volume-weighted values probed by the density diagnostics used in this work. We, therefore, attribute the observed Hα excess to collisional enhancement.

Accordingly, we adopted the reddening derived from Hγ/Hβ, $E(B-V) = 0.052^{+0.110}_{-0.052}$ mag using J. A. Cardelli et al. (1989) (the D. Calzetti et al. (2000) value is similar at $E(B-V) = 0.050 \pm 0.1215$ mag), and corrected all emission lines for the resulting (minimal) dust attenuation. We used the D. Calzetti et al. (2000) reddening law for the rest-UV emission lines ($\lambda < 3200$ Å) and the J. A. Cardelli et al. (1989) reddening law for the rest-optical emission lines ($\lambda > 3200$ Å). After applying the reddening correction, the Hα/Hβ ratio still shows a collisional excess of 0.204 above the theoretical value; we correct for this excess and report a final $F_{\mathrm{H}\alpha} = 1.985 \times 10^{-17}$ erg s^{-1} cm^{-2}.

The adopted reddening and dereddened line intensities are listed in Table 2 for all line fluxes used in this work. Note that rest-UV and rest-optical lines should not be compared or combined in line ratios. Since the rest-UV and rest-optical spectra were obtained during different observing runs with distinct pointings and strategies, we report the UV lines relative to $F_{\mathrm{CIII]}\lambda\lambda1907,1909} \times 100$ and the optical lines relative to $F_{\mathrm{H}\beta} \times 100$, without applying any relative scalings between the two datasets.

3. Wolf Rayet Stars at $z = 6.1$

The WR stage of massive star evolution is an important, short-lived phase that can have significant effects on the chemical composition of the local ISM. We provide a brief overview here (see, e.g., P. A. Crowther 2007, for a more thorough review). WR stars are massive stars that have entered the core He-burning phase and have lost their outer envelope either via strong stellar winds or due to binarity effects (i.e., stripping via Roche Lobe overflow or mergers). The first phase of WR stars occurs when the outer H layer has been ejected, revealing the H core-burning products such that their spectra are characteristically He and N rich but are H-poor. Such stars are known as nitrogen-type WR, or WN, stars, and are often identified by strong N III, N IV, and N V emission lines, especially the broad optical "blue bump" near λ4650. The blue bump is a complex of features, including N III $\lambda\lambda$4634,4642, C III λ4649,4667, Fe III λ4660, and He II λ4687. Subsequently, stars that are massive enough for core He-burning and for their winds to remove their outer He envelope and expose the produced C enter the WR carbon (WC) phase. WC stars also have strong, broad He II emission and strong C and O emission, such that they are identified by the optical WR C IV $\lambda\lambda$5803,5814 doublet (the "red bump"). As a result, the typically very strong winds of the WR phase can produce significant N enrichment during the WN phase and drive strong C ejection during the WC phase. After the WC phase, a WR-oxygen phase may ensue, but we forgo discussion of this phase here.

The rest-frame UV and optical spectra shown in Figure 2 can be used to characterize the WR nature of the stellar population in RXCJ2248-ID3. Both the UV and optical He II emission features are kinematically broadened compared to the

Table 3
Nebular Conditions and Abundances for RXCJ2248-ID3

Property	Ion. E (eV)	Used	Value
Temperatures:			
$T_{e,\mathrm{high}}$ meas. (K)	35.11–54.93	$n_e(\mathrm{N}^{+3})$	$1.97 \pm 0.03 \times 10^4$
$T_{e,\mathrm{int.}}$ used (K)	23.33–34.83	D. R. Garnett (1992)	$1.81 \pm 0.02 \times 10^4$
$T_{e,\mathrm{low}}$ used (K)	13.62–35.11	D. R. Garnett (1992)	$1.68 \pm 0.02 \times 10^4$
Densities:			
$n_e(\mathrm{N}^{+3})$ (cm^{-3})	47.45–77.47	$T_{e,\mathrm{high}}$	$2.65^{+0.45}_{-0.38} \times 10^5$
$n_e(\mathrm{Ar}^{+3})$ (cm^{-3})	40.74–59.81	$T_{e,\mathrm{high}}$	$1.75^{+0.26}_{-0.22} \times 10^4$
$n_e(\mathrm{C}^{+2})$ (cm^{-3})	24.38–47.89	$T_{e,\mathrm{int.}}$	$7.94^{+0.69}_{-0.65} \times 10^4$
$n_e(\mathrm{Si}^{+2})$ (cm^{-3})	16.35–33.49	$T_{e,\mathrm{int.}}$	$4.77^{+5.68}_{-2.33} \times 10^4$
$n_e(\mathrm{S}^{+})$ (cm^{-3})	10.36–23.33	$T_{e,\mathrm{low}}$	$1.15^{+2.23}_{-0.69} \times 10^3$
O Abundances:			
$\mathrm{O}^+/\mathrm{H}^+$ ($\times 10^{-5}$)	13.62–35.11	$T_{e,\mathrm{low}}$; $n_e(\mathrm{Si}^{+2})$	0.186 ± 0.148
$\mathrm{O}^{+2}/\mathrm{H}^+$ ($\times 10^{-5}$)	35.11–54.93	$T_{e,\mathrm{high}}$; $n_e(\mathrm{Ar}^{+2})$	5.473 ± 0.261
12 + log(O/H)			7.753 ± 0.023
Ionization Parameters:			
$\log U_{\mathrm{int.}}(\mathrm{O}_{32})$	13.62–54.93	$n_e = 10^4$ cm^{-3}	-1.24 ± 0.23
$\log U_{\mathrm{high}}(\mathrm{N}_{43})$	29.60–77.47	$n_e = 10^5$ cm^{-3}	-0.69 ± 0.10
N Abundances:			
$\mathrm{N}^{+3}/\mathrm{O}^{+2}$	47.45–77.47	$T_{e,\mathrm{high}}$; $n_e(\mathrm{N}^{+3})$	0.277 ± 0.043
$\mathrm{N}^{+2}/\mathrm{O}^{+2}$	29.60–47.45	$T_{e,\mathrm{high}}$; $n_e(\mathrm{C}^{+2})$	0.145 ± 0.070
$\mathrm{N}^{+}/\mathrm{O}^{+}$	14.53–29.60	$T_{e,\mathrm{low}}$; $n_e(\mathrm{Si}^{+2})$	0.367 ± 0.259
ICF($\mathrm{N}^{+3}/\mathrm{O}^{+2}$)	47.45–77.47	$T_{e,\mathrm{high}}$; $n_e(\mathrm{N}^{+3})$	1.542
ICF($\mathrm{N}^{+2}/\mathrm{O}^{+2}$)	29.60–47.45	$T_{e,\mathrm{high}}$; $n_e(\mathrm{C}^{+2})$	2.547
ICF($\mathrm{N}^{+}/\mathrm{O}^{+}$)	14.53–29.60	$T_{e,\mathrm{low}}$; $n_e(\mathrm{Si}^{+2})$	0.814
$\log(\mathrm{N/O})_{\mathrm{N}^{+3}}$	⋯	⋯	-0.368 ± 0.062
$\log(\mathrm{N/O})_{\mathrm{N}^{+2}}$	⋯	⋯	-0.434 ± 0.071
$\log(\mathrm{N/O})_{\mathrm{N}^{+}}$	⋯	⋯	-0.525 ± 0.257
$\log(\mathrm{N/O})_{\mathrm{all}}$	⋯	⋯	-0.375 ± 0.056
$\langle \log(\mathrm{N/O}) \rangle$	⋯	⋯	-0.390 ± 0.035
C Abundance:			
$\mathrm{C}^{+2}/\mathrm{O}^{+2}$	24.38–47.89	$T_{e,\mathrm{int}}$; $n_e(\mathrm{C}^{+2})$	0.107 ± 0.014
ICF($\mathrm{C}^{+2}/\mathrm{O}^{+2}$)	24.38–47.89	$T_{e,\mathrm{int}}$; $n_e(\mathrm{C}^{+2})$	1.498
log(C/O)			-0.795 ± 0.052
Si Abundance:			
$\mathrm{Si}^{+2}/\mathrm{O}^{+2}$	16.35–33.49	$T_{e,\mathrm{low}}$; $n_e(\mathrm{Si}^{+2})$	0.005 ± 0.001
ICF($\mathrm{Si}^{+2}/\mathrm{O}^{+2}$)	16.35–33.49	$T_{e,\mathrm{low}}$; $n_e(\mathrm{Si}^{+2})$	3.507
log(Si/O)	⋯	⋯	-1.781 ± 0.157

Note. Ionic and total abundances for RXCJ2248-ID3. Column (1) lists the property, while Column (2) lists the associated ionization potential energy range (eV), Column (3) lists the temperature and/or density used in the calculation, and Column (4) provides the final values. All calculations reported here only used the narrow components when multicomponent fits were performed. Note that the temperatures for the intermediate- and low-ionization zones were inferred from $T_{e,\mathrm{high}}$ using the T_e–T_e relationships of D. R. Garnett (1992). Two ionization parameters are reported for the O_{32} and N_{43} indicators from Z. Martinez et al. (2025). The oxygen abundance was determined using the archival [O II] λ3728 detection and the new [O III] λ5008 fit. N/O was determined using four different ion+ICF (from Z. Martinez et al. 2025) combinations: (1) optical $\mathrm{N}^+/\mathrm{O}^+$; (2) UV $\mathrm{N}^{+2}/\mathrm{O}^{+2}$; (3) UV $\mathrm{N}^{+3}/\mathrm{O}^{+2}$; and (4) combination $(\mathrm{N}^+ + \mathrm{N}^{+2} + \mathrm{N}^{+3})/(\mathrm{O}^+ + \mathrm{O}^{+2})$. C/O and Si/O were determined from the archival UV emission lines only.

narrow nebular emission features in RXCJ2248-ID3, indicative of WR or VMS winds. F. Martins et al. (2023, 2025) have shown that young star-forming regions dominated by VMSs can be distinguished from WR stars using the morphology of the blue and red bumps. In particular, VMSs produce blue bumps with He II λ4687 emission but little to no N III emission and red bumps with narrow C IV λλ5803,5814 emission. Thus, strong detections of N III in the blue bump favor a WN interpretation (e.g., F. Martins et al. 2023; D. A. Berg et al. 2024; T. E. Rivera-Thorsen et al. 2024).

The upper right-hand panel of Figure 2 highlights the blue bump spectral regime, showing weak, broad He II and N III λ4642 in RXCJ2248-ID3, both of which are characteristic of metal-poor WN stars. Just redward of the N III λ4642 line in the blue bump (but blueward of [Fe III]), a second less prominent emission feature is seen, but it is difficult to determine whether this is due to C III or O II emission, or both. Furthermore, the red C IV bump is not detected, suggesting little to no contributions from WC stars or VMSs in the spectrum. Thus, we only significantly detect the blue WR bump, suggesting that WN stars are likely present.

4. Nebular Properties

Using the updated narrow-component emission-line fits presented in Section 2.2, we determined the nebular properties of RXCJ2248-ID3. Following D. A. Berg et al. (2021), we adopt the four-zone ionization model to account for the high-ionization emission observed. In this model, the ionization potential energy ranges of N^+, S^{+2}, O^{+2}, and He^{+2} define the low-, intermediate-, high-, and very high-ionization zones, respectively. For all calculations, we use the `PyNeb` package in `Python` with the atomic data adopted in D. A. Berg et al. (2019), which includes a six-level atom model for oxygen in order to utilize the UV O III] λ1666 line. Below, we determine temperatures and densities, although $T_e(\mathrm{O}^{+2})$ and $n_e(\mathrm{N}^{+3})$ were codetermined during the iterative reddening calculation (see Section 2.3) in Section 4.1, ionization parameters in Section 4.2, and abundances in Section 4.3.

We note that the UV spectra do not have sufficient S/N to decompose narrow and broad components following the same method as the optical lines. As a result, density diagnostics and abundances determined from UV lines may include contributions from multiple kinematic components, while optical temperatures, densities, and abundances are derived from narrow components alone. If the broad component arises from gas with distinct physical conditions, this could introduce systematic offsets. For this reason, we examine the potential impact of UV broad components in Section 4.4.

4.1. Temperature and Density

One of the unique characteristics of RXCJ2248-ID3 is its large number of density-sensitive emission-line ratios. M. W. Topping et al. (2024) previously reported densities from the three UV line ratios of Si III] λ1883/λ1892, characterizing the intermediate-ionization zone, C III] λ1907/λ1909, characterizing the intermediate- to high-ionization zone, and N IV] λ1483/λ1486, characterizing the high- to very high-ionization zone. The new high-S/N optical spectra enables us to measure, for the first time, densities from the low-ionization [S II] λ6717/6731 ratio and the high- to very high-ionization [Ar IV] λ4713/λ4741 ratio.

We use our narrow-component dereddened flux measurements to compute densities for all five line ratios and the high-ionization zone temperature from the [O III] λ4364/λ5008 ratio. The high-ionization zones $T_e(\mathrm{O}^{+2})$ and $n_e(\mathrm{N}^{+3})$ were simultaneously determined during the iterative reddening calculation in Section 2.3 to account for the sensitivities of both diagnostics. If the low density limit was assumed instead ($n_e \lesssim 10^2$ cm^{-3}), as is common practice at low-redshift, the observed [O III] $\lambda4364/\lambda5008$ flux ratio would lead to unphysical temperatures (i.e., above the limit set by H cooling of $\sim 2.5 \times 10^4$ K). Thus, a physical and robust solution requires high densities to properly account for the reduced $\lambda5008$ flux due to collisional de-excitation. Furthermore, Z. Martinez et al. (2025) recently showed that densities derived from both optical and UV diagnostics underpredict the true volume-averaged density in multiphase, high-density systems, with more severe underprediction from the optical diagnostics. Therefore, it is necessary to use UV density diagnostics in high-density environments, though the true density will still be underestimated in multiphase gas (see, e.g., Figure 11 of Z. Martinez et al. 2025).

For the high-ionization zone, we found a $T_e(\mathrm{O}^{+2}) = 1.97 \pm 0.03 \times 10^4$ K and $n_e(\mathrm{N}^{+3}) = 2.65^{+0.39}_{-0.37} \times 10^5$ cm^{-3}, which is consistent with the density of $n_e(\mathrm{N}^{+3}) = 3.1^{+0.5}_{-0.4} \times 10^5$ cm^{-3} reported by M. W. Topping et al. (2024), but lower than their temperature of $2.46 \pm 0.26 \times 10^4$ K due to our broad component fits of both [O III] $\lambda4364$ and $\lambda5008$. Adopting our $T_e(\mathrm{O}^{+2})$ as the high-ionization temperature ($T_{e,\mathrm{high}}$), we then applied the T_e–T_e relations of D. R. Garnett (1992) to estimate the intermediate-ionization temperature ($T_{e,\mathrm{int.}}$) and low-ionization temperature ($T_{e,\mathrm{low}}$).

The determined temperatures were used for the subsequent density calculations in their respective ionization zones. Note that the [Ar IV] $\lambda4713$ and He I $\lambda4714$ lines are blended in the G395M grating. Therefore, we corrected the [Ar IV] $\lambda4713$ flux for the He I $\lambda4714$ contribution, predicting the He I $\lambda4714$ flux from the measured He I $\lambda4473$ flux and the theoretical He I $\lambda4714/\lambda4473$ ratio ($\sim$0.21 for the conditions in RXCJ2248-ID). The resulting densities, all of which fall within their respective diagnostic ranges, and temperatures are reported in Table 2.

Remarkably, RXCJ2248-ID3 is one of few galaxies, and the only galaxy yet at high redshifts, to have significant ($>3\sigma$) electron density measurements from five different ions that span a large ionization range ($\sim$10–77 eV). Furthermore, the densities in RXCJ2248-ID3 appear to be organized into an interesting nebular stratification. The UV emission lines trace the densest gas, with $n_e(\mathrm{N}^{+3}) = 2.65 \times 10^5$ cm^{-3} in the highest-ionization gas, followed by $n_e(\mathrm{C}^{+2}) = 7.94 \times 10^4$ cm^{-3} and $n_e(\mathrm{Si}^{+2}) = 4.77 \times 10^4$ cm^{-3}. In contrast, the optical high-ionization lines are emitted from regions of lower densities: the optical [Ar IV] diagnostic has an overlapping ionization energy range with the UV N IV] diagnostic but a density that is an order of magnitude lower.

There are two possible interpretations of the measured array of densities. First, since the UV lines also have higher excitation energies, they could originate preferentially from hotter, denser clumps. This would imply a strongly inhomogeneous ISM, in which compact, high-pressure structures dominate the UV line emission while somewhat more diffuse gas produces much of the optical emission. Alternatively, the multiphase ISM may span a smaller dynamic range of densities than we measure due to the suppression of the optical diagnostics. Z. Martinez et al. (2025) showed that for an ISM with a mix of low- (e.g., 10^3 cm^{-3}) and high-density gas (e.g., 10^5 cm^{-3}) that has a true volumetric density that is somewhere in between, the low-ionization optical diagnostics will always be significantly biased low, close to the low-density gas value, until the fraction of high-density gas is very high (e.g., >95%). This effect occurs when n_e-diagnostic line ratios have low critical densities (e.g., $n_{e,\mathrm{crit}}$([S II])$\approx 2 \times 10^3$–5×10^3 cm^{-3}), such that emission from the high-density gas is collisionally suppressed beyond detection. The magnitude of this effect decreases with increasing critical density such that [S II] is significantly affected, [Ar IV] is moderately affected ($n_{e,\mathrm{crit}} \approx 2 \times 10^4$–$2 \times 10^5$ cm^{-3}), and the UV Si III], C III], and N IV] ($n_{e,\mathrm{crit}} \approx 5 \times 10^4$–$5 \times 10^{10}$ cm^{-3}) are minimally affected, albeit still biased low. In this scenario, there would still be density stratification, but with smaller differences.

All together, the nebular diagnostics in RXCJ2248-ID3 support a picture of a multiphase nebula with density and temperature stratification, likely reflecting a clumpy ISM shaped by the feedback and local radiation field variations of bursty star formation (see, also, N. Choustikov et al. 2025; Y. Harikane et al. 2025b; M. Usui et al. 2025). This picture is also consistent with the density stratification that has been reported for dwarf galaxies both near and far (e.g., B. L. James et al. 2016; D. A. Berg et al. 2021; M. Mingozzi et al. 2022; X. Ji et al. 2024; M. W. Topping et al. 2024), but with typical densities increasing with redshift (e.g., Y. Isobe et al. 2023; Abdurro'uf et al. 2024; Z. Martinez et al. 2025; M. W. Topping et al. 2025a).

4.2. Ionization Parameter

The ionization parameter of RXCJ2248-ID3, $\log U$, determined using the typical $\mathrm{O}_{32} = I_{\lambda5008}/I_{\lambda3728}$ diagnostic is reported in M. W. Topping et al. (2024) to be in the high range of $\log U = -0.5$ to -1. We recompute the ionization parameter for RXCJ2248-ID3 using the O_{32} and $\mathrm{N}_{43} = I_{\lambda\lambda1483,1486}/I_{\lambda1750}$ diagnostics from Z. Martinez et al. (2025) that are calibrated for densities in the $10^2 \leqslant n_e(\mathrm{cm}^{-3}) \leqslant 10^6$ range. We estimate a $\log U_{\mathrm{int}} = -1.24 \pm 0.23$ using O_{32}, which is consistent with the value reported by M. W. Topping et al. (2024), and $\log U_{\mathrm{high}} = -0.69 \pm 0.23$ using N_{43}. Note, however, that the O_{32} diagnostic is very sensitive to the assumed density (Z. Martinez et al. 2025), making this value highly uncertain in dense gas. For example, densities of $n_e = 10^3$–10^5 cm^{-3} would lead to a range of $\log U_{\mathrm{int}} = -0.57$ to -2.04, respectively.

4.3. Abundances

Here, we present direct-method abundances of oxygen-to-hydrogen (O/H) (Section 4.3.1), N/O (Section 4.3.2), carbon-to-oxygen (C/O) (Section 4.3.3), and silicon-to-oxygen (Si/O) (Section 4.3.4) for RXCJ2248-ID3 using narrow-line flux ratios and the measured temperatures and densities presented in Section 4.1. Nearly all of the optical lines used in this work have sufficient S/N to simultaneously constrain broad and narrow emission components, but there are a few exceptions, all of which are low-ionization lines. The [O II] $\lambda3728$ line was not covered by the GLIMPSE-D spectrum and so lacks the S/N to fit broad components. Both [N II] $\lambda6585$ and [S II] $\lambda\lambda6718,6733$ are covered in the high-S/N GLIMPSE-D spectrum but are either blended with stronger features or too weak to fit broad components. On the other hand, the [O II] and [S II] lines have low critical densities around $n_{e,\mathrm{crit}} \sim 10^3$ cm^{-3} such that any moderate to high-density broad components are likely collisionally de-excited away. Their narrow-component fluxes could also be significantly reduced by collisional de-excitation; however, the missing [O II] emission is likely small in the absolute sense for such a high-ionization object. Emission from [N II] is less likely to be collisionally de-excited ($n_{e,\rm crit} \sim 10^5$ cm^{-3}), so a hidden broad component could lead to an overestimate of the N/O abundance, but this effect would be somewhat countered by the underestimated [O II] flux. In the end, the consistency of N/O derived independently from UV and optical tracers in Section 4.3.2 below suggests that these effects do not significantly impact our results.

To calculate the total or relative abundance of an element, we determine and sum the individual observed ions and then apply an ionization correction factor to account for unseen prominent ionization states. The abundance of an individual ionic species, X^i, relative to hydrogen is determined as

$$\frac{N(X^i)}{N(H^+)} = \frac{I_{\lambda(i)}}{I_{\rm H\beta}}\frac{j_{\rm H\beta}}{j_{\lambda(i)}}, \tag{1}$$

where $j_{\lambda(i)}$ is the emissivity determined for the appropriate ionization zone temperature and density. Given the tendency of the optical density diagnostics to severely underestimate the density in high-density environments, we instead adopt the UV-derived densities. Note that the abundances presented below have not been corrected for the fraction of atoms embedded in dust. However, the level of depletion onto dust grains is expected to be small for the low metallicity of RXCJ2248-ID3 (e.g., A. Rémy-Ruyer et al. 2014; F. Galliano et al. 2018; J. Roman-Duval et al. 2022). Y. Isobe et al. (2026) also infer negligible dust depletion for RXCJ2248-ID3 based on the high value of Si/O that that they determine, but this is inconsistent with the value we determine below. Details of elemental abundance determinations are given below.

4.3.1. Oxygen Abundance

We determine the total O/H abundance as the sum of the O^+/H^+ and O^{+2}/H^+ ionic abundances, determined from the [O II] λ3728 and [O III] $\lambda\lambda$4960,5008 optical emission lines. We observe no strong O^0 or O^{+3} emission, indicating that contributions from other ions are negligible. The resulting ionic and total oxygen abundances are presented in Table 2. Similar to M. J. Hayes et al. (2025) and Z. Martinez et al. (2025), we find that one of the most significant effects of accounting for high densities is the resulting decrease in electron temperature and subsequent increase in oxygen abundance (see, also, H. Katz et al. 2023). In our work, this results both from accounting for the missing [O III] λ5008 flux due to collisional de-excitation and from correcting the narrow emission for broad emission components at their base. M. W. Topping et al. (2024) also incorporated the high densities seen in RXCJ2248-ID3 but did not have the S/N to fit the broad emission components in both [O III] λ5008 and λ4364. As a result, we measure an oxygen abundance of $12 + \log(\rm O/H) = 7.753 \pm 0.025$. Note that if unresolved high-density clumps ($n_e \gtrsim 10^5$ cm^{-3}) are present (as suggested in, e.g., Section 2.3), it could introduce additional uncertainty by biasing the luminosity-weighted [O III] $\lambda4364/\lambda5008$ ratio to higher densities, which would drive the derived T_e higher and O/H abundance lower. However, Z. Martinez et al. (2025, see Figure 11), showed that the use of high-critical density UV density diagnostics largely mitigate this effect in a density stratified medium.

4.3.2. Relative N/O Abundance

The extraordinary simultaneous detections of [N II] λ6585, N III] λ1750, and N IV] $\lambda\lambda$1483,1487 enable multiple determinations of the N/O abundance. Therefore, we calculate N/O abundances using four different ionic methods

$$1.\quad \frac{\rm N}{\rm O} = \frac{\rm N^+}{\rm O^+} \times {\rm ICF} = \frac{\rm N^+}{\rm O^+} \times \left[\frac{X(\rm N^+)}{X(\rm O^+)}\right]^{-1}, \tag{2}$$

$$2.\quad \frac{\rm N}{\rm O} = \frac{\rm N^{+2}}{\rm O^{+2}} \times {\rm ICF} = \frac{\rm N^{+2}}{\rm O^{+2}}\left[\frac{X(\rm N^{+2})}{X(\rm O^{+2})}\right]^{-1}, \tag{3}$$

$$3.\quad \frac{\rm N}{\rm O} = \frac{\rm N^{+3}}{\rm O^{+2}} \times {\rm ICF} = \frac{\rm N^{+3}}{\rm O^{+2}}\left[\frac{X(\rm N^{+3})}{X(\rm O^{+2})}\right]^{-1}, \tag{4}$$

$$4.\quad \frac{\rm N}{\rm O} = \frac{\rm N^+ + N^{+2} + N^{+3}}{\rm O^+ + O^{+2}}, \tag{5}$$

where [O II] λ3728 is used for the N^+/O^+ determination, O III] λ1666 is used for the N^{+2}/O^{+2} and N^{+3}/O^{+2} calculations, and $X(N^{+i})$ and $X(O^{+i})$ are the N and O ionization fractions, respectively. We use the density-dependent ICFs from Z. Martinez et al. (2025), who provide prescriptions for densities of $n_e = 10^2$, 10^3, 10^4, 10^5, and 10^6 cm^{-3}. We, therefore, round our density measurements to the nearest order of magnitude and use the intermediate-ionization $\log U$ for the N^+/O^+ ICF and the high-ionization $\log U$ for the N^{+2}/O^{+2} and N^{+3}/O^{+2} ICFs. The resulting N ICFs and N/O abundances are reported in Table 3.

The four N/O determinations of RXCJ2248-ID3 are in close agreement, far above the expected value for its metallicity. Visually, this is shown in the upper left-hand panel of Figure 4, which plots the relative N/O versus O/H abundance with RXCJ2248-ID3 marked by purple diamonds. The traditional N/O–O/H trend has been established by many $z \sim 0$ studies of H II regions and galaxies (gray points: C. Esteban et al. 2002, 2009, 2014; L. S. Pilyugin & T. X. Thuan 2005; L. van Zee & M. Haynes 2006; J. García-Rojas & C. Esteban 2007; Á. R. López-Sánchez et al. 2007; D. A. Berg et al. 2012, 2016, 2019, 2020). The empirical trend is a bimodal relationship, with a flat trend due to primary (or metallicity-independent) N production at low metallicities ($12 + \log(\rm O/H) \lesssim 8.0$) and an increasing N/O trend with O/H as secondary (or metallicity-dependent) N production becomes increasingly important at higher metallicities ($12 + \log(\rm O/H) \gtrsim 8.0$). As a visual guide, the primary N/O plateau from D. A. Berg et al. (2019, dashed purple line) is shown and the empirical stellar curve from D. C. Nicholls et al. (2017, solid green line) is shown as an example of the full primary and secondary curve.

For comparison, we plot the high-quality high-redshift N/O measurements that were calculated in a consistent manner as the present work (with direct-method T_e and n_e determinations and n_e-dependent ICFs) by Z. Martinez et al. (2025). N/O abundances determined using N^{+2}/O^{+2} are plotted as blue + symbols, while N^+/O^+ determinations are plotted as blue pentagons. Of these galaxies, the closest comparison to RXCJ2248-ID3 is CEERS-1019 (see, also, R. Marques-Chaves et al. 2024), while only GDS 3073 and GN-z11 have higher relative N/O abundances and only GDS 3073 is more enhanced in N/O for its O/H abundance.

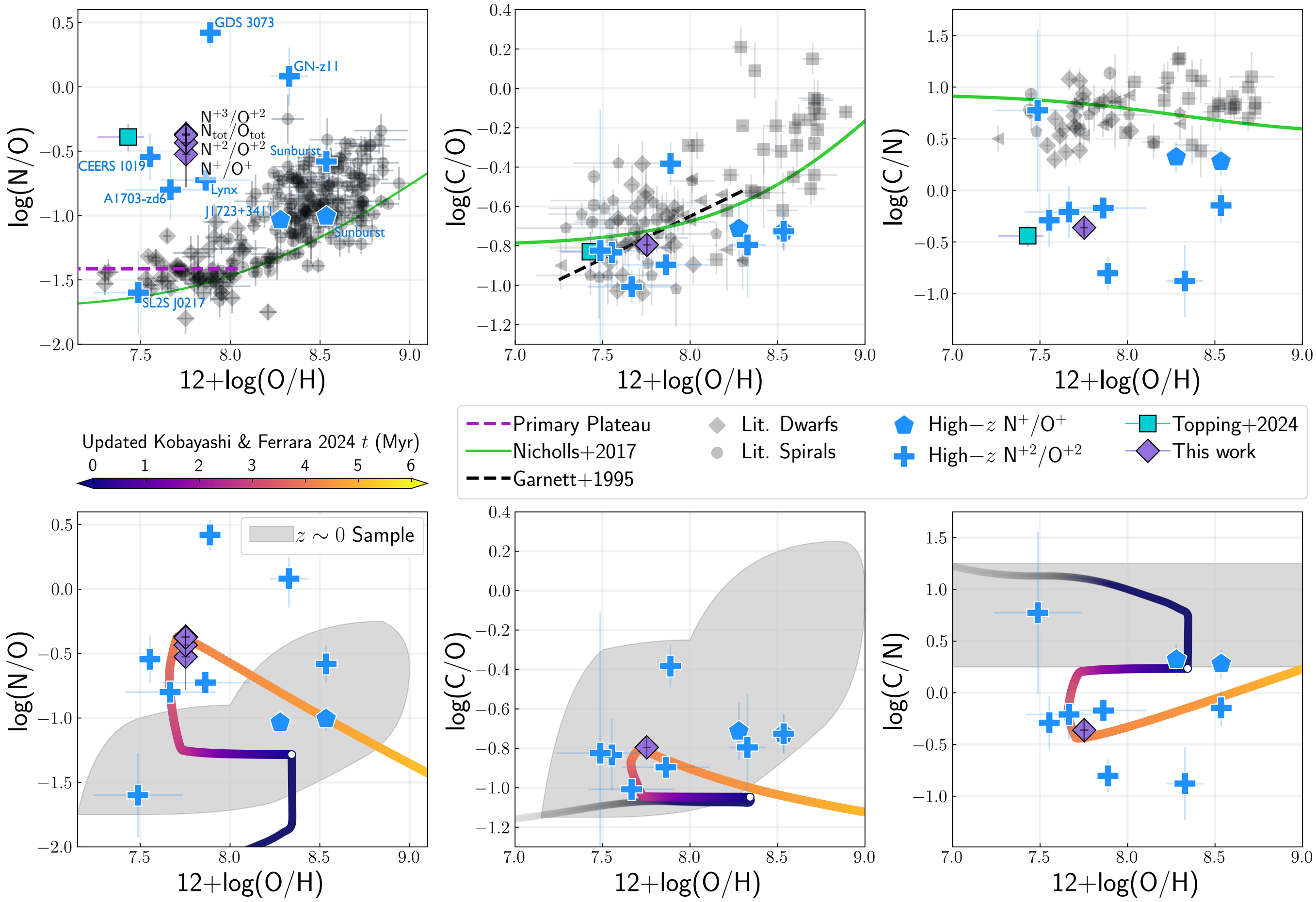

Figure 4. Relative C and N abundance trends versus metallicity. Nitrogen to oxygen ratio versus oxygen abundance for star-forming galaxies is plotted in the left panels, while C/O ratio versus oxygen abundance is plotted in the middle panels, and carbon to nitrogen abundance versus oxygen abundance is plotted in the right panels. Top row: RXCJ2248-ID3 is shown relative to the observed $z \sim 0$ trend and other high-z galaxies. The abundances for RXCJ2248-ID3 are shown as purple diamonds, where multiple N/O points show the measurements for each ionic N/O calculation method. For comparison, we also plot the abundances derived for RXCJ2248-ID3 by M. W. Topping et al. (2024) as turquoise squares. The typical bimodal N/O trend is characterized by local dwarf (gray diamonds; L. van Zee & M. Haynes 2006; D. A. Berg et al. 2012, 2016, 2019) and spiral galaxy (gray circles; C. Esteban et al. 2002, 2009, 2014; L. S. Pilyugin & T. X. Thuan 2005; J. García-Rojas & C. Esteban 2007; Á. R. López-Sánchez et al. 2007; D. A. Berg et al. 2020) H II region measurements. The primary N/O plateau from D. A. Berg et al. (2019) is shown as a dashed purple line, while the solid green line is the empirical stellar curve from D. C. Nicholls et al. (2017). Additional C/O literature measurements for dwarf galaxies are from M. A. Peña-Guerrero et al. (2017) and P. Senchyna et al. (2017). Abundances for $z > 2$ galaxies from Z. Martinez et al. (2025) are plotted as blue plus signs for galaxies with UV N^{+2}/O^{+2} derived abundances and pentagons for optical N^{+}/O^{+} derived abundances. Bottom row: The same observed samples are shown as the top row, but with the $z \sim 0$ sample represented by the shaded gray regions. The observed abundances of RXCJ2248-ID3 are compared to updated dual-burst chemical evolution models of C. Kobayashi & A. Ferrara (2024, string of circles), color coded by age since onset of the second burst. The models have been modified to reproduce both the enhanced N/O and relatively deficient C/O observed for RXCJ2248-ID3, which requires enrichment from WN but very little WC enrichment, as expected at low metallicities.

We find that all four ionic methods produce consistently high N/O values within their uncertainties, with a weighted mean of $\log(\mathrm{N/O}) = -0.391 \pm 0.037$. This is an important result because RXCJ2248-ID3 is the first galaxy to have consistently enhanced N/O abundances measured from both the rest-frame UV high-ionization and the optical low-ionization emission lines. Furthermore, measuring consistent N/O values from three different ionic methods strengthens our confidence in the robustness of the N/O measurement, although uniform N/O across the ionization structure of the nebula is not a given in a stratified medium. While there is strong evidence for a stratified, or perhaps very clumpy, density structure in RXCJ2248-ID, the N/O abundance appears to be well mixed.

4.3.3. Relative C/O Abundance

Measuring the C/O abundance provides a crucial comparative baseline for interpreting the origin of elevated N/O in RXCJ2248-ID3. Similar to N, C has a pseudosecondary[17] production pathway, but the dominant nucleosynthetic sources and timescales differ for C and N. Briefly, both C and O are primarily produced in massive stars ($>8\,M_\odot$) on relatively short timescales such that the C/O ratio is a relatively stable tracer of massive star yields, although some C is produced via low- to intermediate-mass AGB stars ($\sim$1.5–3 $M_\odot$). In contrast, some N is produced by massive stars (e.g., through rotational mixing and WR winds) but most N comes from intermediate-mass AGB stars ($\sim$4–8 $M_\odot$), which release N on longer timescales ($\sim$200 Myr). Therefore, N/O and C/O together serve as diagnostics of the recent star formation

---

[17] There are no known secondary nucleosynthetic production methods for C; only the primary triple-α process is known to produce C. However, other processes, such as metal-dependent line-drive stellar winds, may be responsible for the empirical increasing trend in C/O–OH, hence the term *pseudosecondary*.

history, constraining the recent enrichment mechanisms of galaxies (e.g., D. R. Garnett 1990; R. B. C. Henry et al. 2000; C. Chiappini et al. 2003; E. Pérez-Montero & T. Contini 2009; D. A. Berg et al. 2019; E. Pérez-Montero et al. 2021).

Relative C/O abundances are typically determined using the C III] $\lambda\lambda$1907,1909/O III] λ1666 ratio to calculate C^{+2}/O^{+2} and assuming that $C/O \approx C^{+2}/O^{+2}$. This method is sometimes used alone owing to the fact that (1) C^{+2} and O^{+2} have somewhat similar ionization potentials (24.38 and 35.12 eV, respectively), (2) the upper levels of the λ1666 and $\lambda\lambda$1907,1909 transitions have similar excitation potentials ($\sim$6.5 and $\sim$7.5 eV, respectively), and (3) the integrated fluxes of λ1666 and $\lambda\lambda$1907,1909 are not sensitive to collisional de-excitation for the densities measured here. However, for the high-ionization nebulae in RXCJ2248-ID3, it is important to account for contributions from the C^{+3} species and any unseen species. We note that the C IV $\lambda\lambda$1548,1550 doublet is clearly observed in the rest-UV spectrum of RXCJ2248-ID3, but these lines are resonant and can be affected by the C IV stellar wind feature and ISM absorption, and so determining the intrinsic flux and subsequent C^{+3} abundance is challenging. Instead, we use an ICF determined from the photoionization models presented in Z. Martinez et al. (2025) such that

$$\frac{C}{O} = \frac{C^{+2}}{O^{+2}} \times \mathrm{ICF} = \frac{C^{+2}}{O^{+2}} \times \left[\frac{X(C^{+2})}{X(O^{+2})}\right]^{-1}. \qquad (6)$$

We used the $\log U_{\mathrm{int.}}$ and a density of $n_e(C^{+2}) \sim 10^5\ \mathrm{cm^{-3}}$ to determine the C ICF. The resulting C ICF and C/O abundance are reported in Table 3.

The C/O and C/N abundances for RXCJ2248-ID3 are plotted in the upper middle and right-hand panels of Figure 4. Empirical trends of C/N at $z \sim 0$ are found to be flat, albeit with significant scatter (see shading in Figure 4), suggesting that the dominant nucleosynthetic mechanisms of C are similar to those of N (e.g., D. R. Garnett et al. 1999; C. Esteban et al. 2014; D. A. Berg et al. 2016, 2019). However, while the production of both C and N appear to be metallicity-dependent, the scatter in their trend is consistent with differing production timescales due to stars of different masses. Thus, the variations observed in CNO abundance patterns of high-redshift galaxies may be the result of taking a snapshot of many galaxies at different times since their most recent onset of star formation.

RXCJ2248-ID3 appears to have a similar CNO abundance pattern to other high-redshift N emitters, characterized by enhanced N/O but relatively deficient C/O such that their C/N is very deficient compared to the expectations from low-redshift trends. This suggests that these high-redshift N-emitting galaxies are enhanced in N relative to both O and C. If massive stars in the WN phase are present, they will have recently produced ^{14}N at the expense of ^{12}C through the CNO cycle, meaning C used as a catalyst in the cycle initiation will have been consumed as N is removed during the bottleneck step via dredged up, preventing the return of C at cycle completion. Thus, C/N-deficiency is consistent with a recent, intense episode of N enrichment and C consumption from WN stars. Conversely, if both N/O and C/O were elevated in tandem, it could point to broader enrichment by massive stars, such as enrichment from both WN and WC stars, whose contributions increase at higher metallicities.

4.3.4. Relative Si/O Abundance

Detecting Si III] $\lambda\lambda$1883,1892 in RXCJ2248-ID3 enables the rare opportunity to measure the silicon-to-oxygen (Si/O) abundance in a $z > 5$ galaxy (see, also, Y. Isobe et al. 2026, for Si/O in GN-z11). Silicon abundances are important for multiple reasons. Silicon is highly refractory, making the Si/O ratio a sensitive probe of dust depletion. Additionally, Si probes different channels of chemical enrichment than CNO elements, as it is primarily an α-element produced by CCSNe, but Type Ia SNe, AGB stars, and even pair-instability SNe are all expected to contribute to the total Si abundance. For RXCJ2248-ID3 we determine the Si/O abundance using the observed Si III] $\lambda\lambda$1883,1892/O III] λ1666 ratio to calculate Si^{+2}/O^{+2}. Because Si^{+2} and O^{+2} have rather different ionization potentials (16.3 eV versus 35.1 eV, respectively), a Si ICF is required to convert Si^{+2}/O^{+2} to total Si/O via

$$\frac{Si}{O} = \frac{Si^{+2}}{O^{+2}} \times \mathrm{ICF} = \frac{Si^{+2}}{O^{+2}} \times \left[\frac{X(Si^{+2})}{X(O^{+2})}\right]^{-1}. \qquad (7)$$

Si ICFs have been reported previously (e.g., D. R. Garnett et al. 1995), but none account for the high-density conditions observed in RXCJ2248-ID3. Therefore, we determined a Si ICF = 3.507 using the photoionization models presented in Z. Martinez et al. (2025) using the $\log U_{\mathrm{int.}}$ and a density of $n_e(Si^{+2}) \sim 10^4\ \mathrm{cm^{-3}}$. Reported in Table 3, the resulting $\log(Si/O) = -1.781 \pm 0.157$ abundance is typical of metal-poor dwarf galaxies (e.g., D. R. Garnett et al. 1995; Y. I. Izotov & T. X. Thuan 1999), consistent with normal massive star production and low dust depletion.

4.4. Potential Impact of UV Broad Components

The exceptionally high S/N of the rest-optical GLIMPSE-D spectrum allows for broad emission component fits that the rest-UV spectrum does not. In Section 2.2, we found the broad emission component contribution to the narrow [O III] λ5008 flux to be 10.8%. To examine the possible effects such contamination has on calculations of nebular conditions and abundances, we adopt 10.8% as the contamination upper limit to the UV emission lines. We first consider the impact on the UV density determinations, where we allow the broad components of the UV density-sensitive emission-line ratios to have densities ranging from 10^2–$10^6\ \mathrm{cm^{-3}}$. After subtracting the potential broad component contribution, the revised densities change up to $\Delta n_e(Si^{+2}) = ^{+0.34}_{-0.67} \times 10^4\ \mathrm{cm^{-3}}$, $\Delta n_e(C^{+2}) = ^{+0.78}_{-0.85} \times 10^4\ \mathrm{cm^{-3}}$, and $\Delta n_e(N^{+3}) = ^{+0.32}_{-0.12} \times 10^5\ \mathrm{cm^{-3}}$ over the range of broad component densities considered. These values are within the reported uncertainties in Table 3, with the exception of the $\sim 1.2\sigma$ deviation for Δn_e of C^{+2}.

Next, we tested the subsequent impact of UV densities that have been revised for possible broad components on the properties determined from rest-optical emission lines: $T_e(O^{+2})$, O/H, and N/O. For the range of $\Delta n_e(N^{+3})$ above, the resulting $\Delta T_{e,\mathrm{high}} = ^{+0.029}_{-0.064} \times 10^4$ K, which is within 1σ–2σ of the reported value in Table 3. Similarly, the impact of the revised densities and temperatures on the oxygen abundance, $\Delta O/H = ^{+0.046}_{-0.017}$ dex, is also within 1σ–2σ. The impact is even smaller for the nitrogen abundance, with $\Delta(N/O)_{N^+} = ^{+0.024}_{-0.038}$ dex being much smaller than the N/O uncertainty.

Relative UV abundances are impacted by changes in both the nebular conditions and the relevant abundance emission-line ratio. However, the resulting abundance deviations are small and within the original uncertainties: $\Delta(\mathrm{N/O})_{\mathrm{N}^{+2}}={}^{+0.005}_{-0.002}$ dex, $\Delta(\mathrm{N/O})_{\mathrm{N}^{+3}}={}^{+0.003}_{-0.001}$ dex, and $\Delta(\mathrm{C/O})={}^{+0.011}_{-0.003}$ dex. Thus, we conclude that while considering the impacts of hidden broad component contributions to the measured UV fluxes is important, the potential biases do not affect the main results or conclusions of this work.

5. A Short Window of Intense WR Nitrogen Enrichment

We have presented evidence for WN stars in RXCJ2248-ID3 in two forms: first, the rest-frame optical WR blue bump discussed in Section 3 and shown in Figure 2; and second, a qualitative comparison of the CNO abundances to patterns expected for WR stars in Section 4.3 and Figure 4. Below, we examine the plausibility and impact of these WN stars by comparing RXCJ2248-ID3 to expected trends for WR stars with metallicity (Section 5.1), testing whether stellar yields can reproduce the observed CNO abundance pattern (Section 5.2) and assessing whether RXCJ2248-ID3's stellar population can produce its inferred mass of ionized N (Section 5.3). Together, these lines of investigation suggest that the enhanced N/O and suppressed C/O in RXCJ2248-ID3 represent a short-lived enrichment phase, unique to metal-poor, highly star-forming galaxies in the early Universe (Section 5.4).

5.1. WN Stars: The Dominant WR Phase at Low Metallicity

To date, no individual resolved WR stars have been directly observed at metallicities as low as RXCJ2248-ID3 ($Z \sim 0.1 Z_\odot$). This is due, in part, to the lack of sufficiently close ($D \lesssim 1$ Mpc for the young, crowded clusters hosting WR stars), metal-poor, star-forming galaxies (see C. Kehrig et al. 2013 for the closest metal-poor WR galaxy), but a scarcity of WR stars in metal-poor environments is also expected because mass loss through stellar winds scales with metallicity. We show the trend of the number of WC/WN stars as a function of metallicity in Figure 5. The observed number of WC/WN stars in M31 ($\sim$175% $Z_\odot$), the Milky Way (MW; $Z_\odot$), M33 ($\sim$40%–110% $Z_\odot$), the Large Magellanic Cloud (LMC; $\sim$40% $Z_\odot$), and the Small Magellanic Cloud (SMC; $\sim$20% $Z_\odot$) suggest that the number of the WN/WC number ratio increases with decreasing metallicity (e.g., G. Meynet & A. Maeder 2005; P. A. Crowther 2007; P. Massey et al. 2015; K. Neugent & P. Massey 2019). This is because weaker metal line-driven winds, rotation, or binary effects in metal-poor stars may be able to expose their nitrogen-rich layers and initiate the WN phase but be insufficient to strip the stellar He atmosphere and reveal the carbon-rich core to initiate the WC phase. Thus, if WR stars form at $Z \sim 10\% Z_\odot$, they are expected to be overwhelmingly WN-type. Additionally, A. A. C. Sander et al. (2026) recently discovered a new class of WN–WO stars that point to a low-metallicity WR evolutionary channel in which stars pass directly from the WN to WO phase, potentially explaining spectra that show evidence for WN-like enrichment and hard ionizing radiation without clear WC signatures.

The spectral features of RXCJ2248-ID3 support the picture of WN star feedback at low metallicity. As shown in Figure 2, the He II emission is moderately broadened, the N III λ4642 line in the blue bump is prominent, and there is no evidence for the red bump C IV feature, all consistent with the presence of WN stars at low metallicity. The weakness of the He II emission in terms of both flux and velocity width is expected for the low-metallicity environment of RXCJ2248-ID3 ($\sim$10% $Z_\odot$) due to reduced wind velocities and mass-loss rates (e.g., A. A. C. Sander et al. 2020). Similarly weak WN features have also been reported in the nearby metal-poor galaxy SBS 0335-052 (Y. I. Izotov et al. 2006) and, at cosmic noon, the $z \sim 2.37$ lensed galaxy the Sunburst Arc (T. E. Rivera-Thorsen et al. 2024) and the $z \sim 2.22$ M4327 galaxy (M. Curti et al. 2025b).

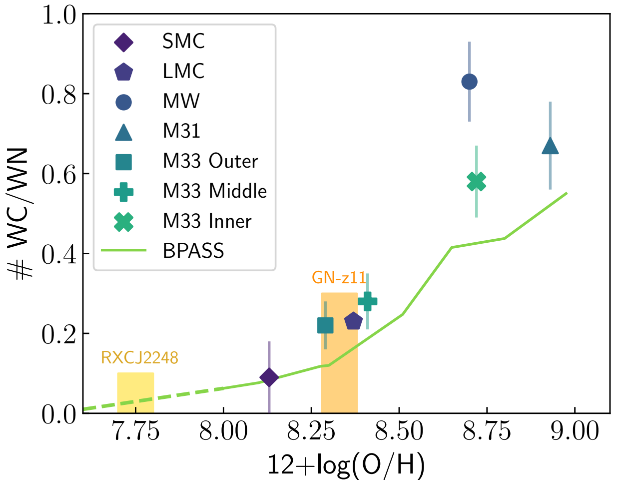

Figure 5. Observed and theoretical ratios of WC/WN star numbers as a function of metallicity. Observed values for the SMC, LMC, MW, and M31 were compiled by K. Neugent & P. Massey (2019), while newer values for M33 come from K. F. Neugent & P. Massey (2023). For comparison, we also plot the trend presented in P. Massey et al. (2017) for BPASS v2.0 binary stellar population synthesis burst models for 12+log(O/H) > 8 (solid line green line), which we extrapolate to lower metallicities (dashed line). Enrichment from WR stars was used to explain the CNO abundances in GN-z11 by C. Kobayashi & A. Ferrara (2024). We note the metallicity for GN-z11 determined by Z. Martinez et al. (2025) is consistent with a WC/WN ratio of $\sim$0.1–0.2 and the metallicity for RXCJ2248-ID3 from the current work, which predicts a much lower WC/WN ratio of $\sim$0.03–0.10. Therefore, very little carbon enrichment from WC stars is expected for RXCJ2248-ID3.

We plot the WR blue bump profile of RXCJ2248-ID3 relative to the Sunburst Arc and M4327 in Figure 6. For ease of comparison, we convolve the Sunburst Arc $R \sim 2700$ JWST/NIRSpec G140H spectrum to the $R \sim 1000$ resolution of the RXCJ2248-ID3 spectrum. For M4327, we retrieved the G140M spectrum obtained as part of the Measuring Abundance at High Redshift with the T_e Approach Survey (MARTA; E. Cataldi et al. 2025) from the Dawn JWST Archive (DJA; K. E. Heintz et al. 2024; A. de Graaff et al. 2025). Both the Sunburst Arc and M4327 spectra were scaled to similar He II strengths as RXCJ2248-ID3. These spectra immediately reveal similar profiles, but with three distinct differences: (1) RXCJ2248-ID3 exhibits higher gas ionization, as evidenced by the strong [Ar IV] $\lambda\lambda$4713,4741 emission; (2) the He II stellar wind feature is significantly broader in both the Sunburst Arc (FWHM = 1370 km s^{-1}) and M4327 (FWHM = 1460 km s^{-1}) than RXCJ2248-ID3 (FWHM = 530 km s^{-1}), consistent with stronger stellar winds at the higher metallicities of the Sunburst Arc: $12 + \log(\mathrm{O/H}) \sim 8.5$ (or $Z \sim 0.7 Z_\odot$; Z. Martinez et al. 2025) and M4327: $12 + \log(\mathrm{O/H}) \sim 8.15$ (or $Z \sim 0.3 Z_\odot$; M. Curti et al. 2025b); and (3) the WR N III λ4642 line is much stronger in RXCJ2248-ID3, which lacks WR C IV $\lambda\lambda$5803,5814 emission, while the Sunburst Arc and M4327 exhibit both N III and C IV emission. These differences support a scenario in which the

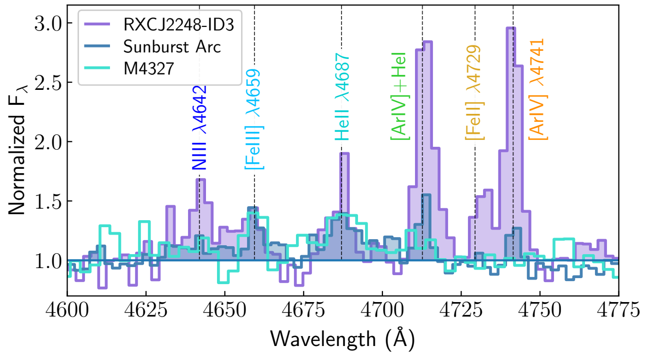

Figure 6. The blue WR region of the optical spectrum of RXCJ2248-ID3 (purple) is shown in comparison to the $z \sim 2.37$ Sunburst Arc spectrum from T. E. Rivera-Thorsen et al. (2024, blue), which has been convolved to $R \sim 1000$ to match RXCJ2248-ID3, and the $z = 2.22$ M4327 spectrum obtained from the DJA, but originally presented in M. Curti et al. (2025b, turquoise). All three galaxies show characteristic signs of hosting WN stars but RXCJ2248-ID3 shows striking N III λ4642 emission that is much stronger than both the Sunburst Arc and M4327. On the other hand, the Sunburst Arc and M4327 show broader He II emission, which is expected for more metal-rich galaxies as stellar winds scale with metallicity.

$z \sim 2$ WR galaxies hosts both WC and WN stars, but the more metal-poor RXCJ2248-ID3 hosts a young population of WN stars with no or very little WC contribution.

5.2. Relative Chemical Enrichment from WN Stars

With the highest redshift detection of WN stars to date, we now explore their chemical yields as a source of the abundance pattern in RXCJ2248-ID3. C. Charbonnel et al. (2023) performed a comparable analysis for the extreme N/O ratio observed in GN-z11 and found that such rapid nitrogen enrichment could arise from normal massive stars with $M_\star \sim 20$–$120\,M_\odot$ or from supermassive stars ($M_\star \gtrsim 1000\,M_\odot$) in protoglobular cluster environments. Their results and those of R. Marques-Chaves et al. (2024) further demonstrated that the short-lived WN-like phase can produce large N/O ratios within a few megayears of the burst, consistent with the timescales inferred here, but that the observed C/O ratios are only compatible over a very short time interval. Building on this theoretical groundwork, C. Kobayashi & A. Ferrara (2024) showed that a dual-burst chemical evolution model with a short WR-dominated enrichment phase could also match GN-z11's enrichment pattern. Similarly, R. Marques-Chaves et al. (2024) used N yields from rotating massive stars to demonstrate that a young, WR-dominated stellar population could reproduce the observed CNO enrichment pattern in CEERS-1019.

The models above provide a valuable physical framework for linking stellar yields to galaxy-scale abundance evolution at early times. To extend the methodologies outlined by these works to RXCJ2248-ID3, we first examine the dual-burst chemical evolution model of C. Kobayashi & A. Ferrara (2024), which was fine-tuned to reproduce the enhanced N/O in GN-z11 (reported by R. Maiolino et al. 2024). This model invokes two bursts of star formation, where the second triggers a narrow ($\lesssim$1 Myr) phase of WR-dominated enrichment. While the model can easily reach the N/O enrichment level of RXCJ2248-ID3, it was also designed to yield the higher O/H and C/O abundances observed in GN-z11 than in RXCJ2248-ID3, which was achieved, in part, by enrichment from WC stars. The updated O/H abundance for GN-z11 determined by Z. Martinez et al. (2025) makes it consistent with some carbon enrichment from WC stars, as shown in Figure 5. However, with a metallicity of only $Z \sim 0.10\,Z_\odot$, the WR population in RXCJ2248-ID3 is expected to consist of few WC stars, and so an updated chemical evolution model is needed to match its unique CNO abundance pattern.

We modify the C. Kobayashi & A. Ferrara (2024) dual-burst model to be more appropriate for the metal-poor conditions in RXCJ2248-ID3. In particular, the galactic chemical evolution (GCE) model uses the same star formation history and the standard IMF (for 0.01–120 $M_\odot$) as in the fiducial model in C. Kobayashi & A. Ferrara (2024) but reduces the contribution from WC stars. C/O ratios of the nucleosynthesis yields vary depending on the uncertain nuclear reaction rates (e.g., ^{12}C(α, γ)^{16}O) and the treatment of convection and mass loss (C. Kobayashi et al. 2006). In the updated model, ^{12}C and ^{16}O yields are taken from C. Kobayashi et al. (2020) for all mass ranges of stars but the contributions from the WC wind phase is scaled to ∼15% in order to match the empirical trends and theoretical expectations that most massive stars will have insufficient winds to remove their He envelopes at such low metallicities.

We plot the updated metal-poor dual-burst model in the bottom row of Figure 4 as a time-series of points that are color coded by the age since the onset of the second burst. In this model, the observed N/O, O/H, and C/O abundances of RXCJ2248-ID3 are reached simultaneously ∼4.2 Myr after the onset of the second burst. This young age is consistent with enrichment from WN stars and with the derived clump age of $1.6^{+11.9}_{-0.9}$ Myr (A. Claeyssens 2025). Thus, the N/O-enhanced and relatively C/O-deficient conditions in RXCJ2248-ID3 are produced by a short-lived evolutionary phase following intense, bursty star formation.

We note that the duration and impact of the WN phase may be significantly extended if the stars evolve in binary systems. In the M. Limongi & A. Chieffi (2018) single-star models, the WN phase typically lasts ∼0.03–0.3 Myr and, due to the metallicity-dependent winds, require high initial masses (∼40 $M_\odot$) to expose the He- and N-rich layers. However, in close binaries, envelope stripping via mass transfer or common-envelope evolution can induce WR phases in lower-mass stars (20–30 $M_\odot$), largely independent of the stellar metallicity. This channel can significantly prolong the WN lifetime (up to ∼1 Myr) depending on the binary mass ratio and separation (e.g., J. J. Eldridge et al. 2017; Y. Götberg et al. 2019; D. R. Aguilera-Dena et al. 2022). As a result, binary evolution may enhance both the frequency and duration of the chemically selective N/O enrichment phase, such as that observed in RXCJ2248-ID. On the other hand, L. Boco et al. (2025) successfully modeled observations of single WR stars in the SMC, suggesting that binary stripping may not be required to produce WR stars at low metallicity. Clearly, the frequency, lifetimes, and formation channels of WR stars in low-metallicity environments are not yet well understood. Future work incorporating current binary and single star WR pathways into chemical evolution models may, therefore, be essential for capturing the full range of nitrogen feedback in low-metallicity starbursts at high redshift.

Taken together, the massive star enrichment scenario presented here, and explored in C. Charbonnel et al. (2023), R. Marques-Chaves et al. (2024), and C. Kobayashi & A. Ferrara (2024), demonstrates that selective enrichment of nitrogen by WN-dominated feedback can naturally reproduce the observed CNO abundance pattern in compact, low-metallicity starbursts such as RXCJ2248-ID3. We can now paint a full picture of the ISM in RXCJ2248-ID3. The consistency of N/O across ions spanning a wide range of ionization potentials suggests that the WN-enriched material has been efficiently mixed throughout the ionized gas. This apparent chemical homogeneity does not contradict the strong density and temperature stratification inferred from our diagnostics: a clumpy or multiphase ISM can remain compositionally uniform if the enriched ejecta are well dispersed. Given the extreme compactness of RXCJ2248-ID3 ($R_e \approx 20$ pc), the characteristic dynamical and sound-crossing times are only a few $\times 10^5$ yr, comparable to or shorter than the duration of the WN phase itself. Under such conditions, turbulent and radiative mixing can rapidly homogenize the heavy-element yields, producing a chemically uniform yet physically structured nebula.

5.3. The N Mass Budget

A crucial point of validation is whether an intense burst of star formation so early in the Universe could have produced the amount of N present in RXCJ2248-ID3. Similar to the analysis in R. Marques-Chaves et al. (2024), we test this by first estimating the ionized nitrogen mass using

$$M_{\rm N_{ion.}} = M_{\rm H_{ion.}} \left(\frac{\rm N}{\rm H}\right)_{\rm ion.} \left(\frac{m_{\rm N}}{m_{\rm H}}\right), \qquad (8)$$

where the atomic mass ratio is $m_{\rm N}/m_{\rm H} = 14$ and N/H is the nitrogen abundance of the ionized gas. The hydrogen gas mass $M_{\rm H}$ is derived from the Hα luminosity as

$$M_{\rm H} = \frac{m_{\rm H} L_{\rm H\alpha}}{h\nu_{\rm H\alpha}\,\alpha^{\rm eff}_{\rm H\alpha}\, n_e}\sqrt{\epsilon}, \qquad (9)$$

where $m_{\rm H} = 1.67 \times 10^{-27}$ kg, $h = 6.626 \times 10^{-27}$ erg s^{-1}, $\nu_{\rm H\alpha}$ is the frequency of the Hα emission line, and $\alpha^{\rm eff}_{\rm H\alpha} = 6.078 \times 10^{-14}$ cm^3 s^{-1} is the Case B effective recombination coefficient for Hα assuming a $T_e = 1.97 \times 10^4$ K. We estimate the Hα luminosity using a luminosity distance of $d_L(z = 6.1025) = 1.817 \times 10^{29}$ cm, the collision-corrected narrow-component Hα flux, and a magnification of $\mu = 6.8877$ (L. Furtak et al. 2025) to be $L_{\rm H\alpha} = 1.20 \times 10^{42}$ erg s^{-1}. Combining this $L_{\rm H\alpha}$ with the equivalent width (EW)(Hα) = 1457 Å, we derive the star formation rate (SFR) using the simulation-based SFR(Hα) calibration from I. G. Kramarenko et al. (2026). This method was developed to be more appropriate for the bursty conditions at high redshift than traditional calibrations and gives SFR = 3.2 $M_\odot$ yr^{-1}, similar to the SED-derived SFRs assuming a constant SFH for 1 Myr (4.7$M_\odot$yr^{-1}) and 10 Myr (4.1$M_\odot$yr^{-1}; see Table 1). Adopting a filling factor of ε = 0.01-0.10, assuming a compact starburst (e.g., R. C. Kennicutt 1984; G. Stasińska & D. Schaerer 1997), a density of 10^4 cm^{-3}, and the measured N/H value, we calculate the ionized nitrogen mass to be $M_{\rm N_{ion.}} \approx 18.2 - 57.5\, M_\odot$.

We then compute the total nitrogen mass that can be produced by the recent burst of star formation using the integrated nitrogen yield produced by the modified C. Kobayashi & A. Ferrara (2024) model for the SED-derived stellar mass of $M_\star = 1.96 \times 10^7 M_\odot$ assuming a continuous SFH over the duration of the second burst (∼4.2 Myr). This results in a total N mass of 435 $M_\odot$, implying that ∼4 − 13% of the gas is retained from the WN winds and ionized when matched to the expected ionized N mass (∼18.2 − 57.5 $M_\odot$) from the crudely calculated observed value. Thus, WN stars formed in a recent burst within a compact, high-density, and very clumpy/inhomogeneous (low-filling-factor) environment can plausibly explain the N mass in RXCJ2248-ID3, even at low metallicity (∼10% $Z_\odot$), without invoking a top-heavy IMF or exotic enrichment channels.

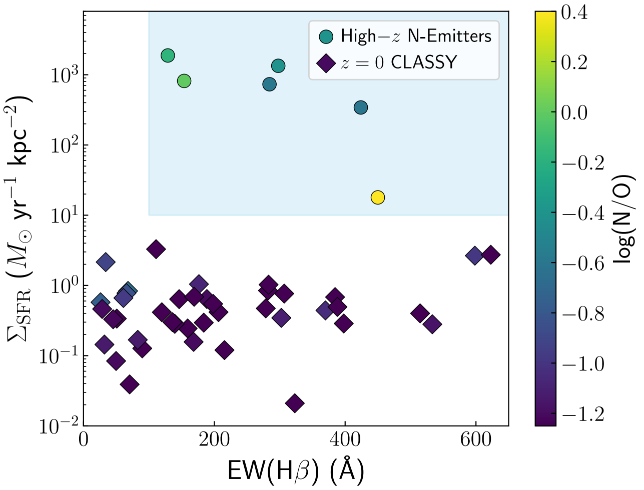

Figure 7. SFR surface density versus Hβ EW for high-redshift ($z > 5$) N emitters versus $z \sim 0$ galaxies from the CLASSY survey (SFR: D. A. Berg et al. 2022; N/O: K. Z. Arellano-Córdova et al. 2025), which have enhanced SFRs similar to $z \sim$ 2–3 galaxies. High-redshift N emitters are only observed at young ages ($\lesssim$5 Myr), as indicated by the high Hβ EWs (EW> 200 Å), and in compact, dense environments ($\Sigma_{\rm SFR} > 10\, M_\odot$ yr^{-1} kpc^{-1}). Note that RXCJ2248-ID3 is plotted here using the properties derived from M. W. Topping et al. (2024) for continuous star formation to be consistent with the other N-emitter measurements.

5.4. The Ephemeral Imprint of WN Star on High−z Galaxies

The prominence of N/O enhancement at $z \gtrsim 5$ but relative rarity in local star-forming galaxies likely reflects a combination of environmental conditions and evolutionary factors that are unique to the early Universe. To examine the likely environments, we plot the SFR surface density ($\Sigma_{\rm SFR}$) versus EW of Hβ in Figure 7 for both $z \gtrsim 6$ N emitters (RXCJ2248-ID3: M. W. Topping et al. 2024, this work; GNz9p4: D. Schaerer et al. 2024; GN-z11, EW(Hβ) inferred from Hγ: A. J. Bunker et al. 2023; S. Tacchella et al. 2023; GDS 3073: E. Vanzella et al. 2010; H. Übler et al. 2023; X. Ji et al. 2024; CEERS-1019: R. L. Larson et al. 2023; R. Marques-Chaves et al. 2024; A1703-zd6: M. W. Topping et al. 2025b) and local star-forming galaxies with enhanced SFRs from the COS Legacy Archive Spectroscopic SurveY (CLASSY; B. L. James et al. 2021; D. A. Berg et al. 2022; N/O from K. Z. Arellano--Córdova et al. 2025). The high-redshift galaxies, such as RXCJ2248-ID3, exhibit compact morphologies ($R_e \lesssim 10^2$ pc) that lead to much higher SFR surface densities than seen at $z \sim 0$, as well as bursty star formation histories that favor the rapid buildup of massive stars capable of entering the short-lived WN phases ($M_\star > 20\, M_\odot$). The high-redshift N emitters also have high Hβ EWs (>200 Å) that are indicative of young current bursts of star formation (<5 Myr). This suggests that compactness alone is not enough to observe enhanced N/O;

we must also observe these galaxies at the fleeting moments of very young bursts when WR stars are most active.

Figure 7 suggests a scenario of elevated N/O at low metallicity being preferentially seen in galaxies with high SFR surface densities and young stellar ages (e.g., D. Schaerer et al. 2024; M. W. Topping et al. 2024; Z. Martinez et al. 2025). R. Marques-Chaves et al. (2024) also suggest that the elevated N/O and high-ionization spectrum of CEERS-1019 trace a short evolutionary window of a $\lesssim$5 Myr burst dominated by WN-like feedback. Furthermore, the theoretical models of C. Charbonnel et al. (2023) predict that such phases are characteristic of young, dense stellar systems, potentially analogous to protoglobular clusters, reinforcing that our observed WN-driven enrichment is a natural outcome of clustered, bursty star formation at early times.

At low metallicity, weaker stellar winds require higher initial masses for stars to reach the WR phase, so a larger total stellar mass must form in a burst to produce a detectable population of WN stars. In compact galaxies beyond cosmic noon, this condition is naturally met in systems with high SFR surface densities, which statistically sample the upper IMF more fully and produce a detectable population of WN stars (e.g., J. Brinchmann et al. 2008; M. Shirazi & J. Brinchmann 2012). Furthermore, the WR enrichment signature is short-lived: it must be captured during the brief WN-dominated phase ($t_{\rm burst} \lesssim 5$ Myr and $\Delta t_{\rm WN} \lesssim 0.3$ Myr), before dilution from WC stars, CCSNe, or delayed AGB enrichment. These timing constraints imply that only a small fraction of the star-forming galaxies in the distant Universe will be caught in this phase. The detection of WR-driven N/O enhancement at high redshift thus reflects a brief evolutionary stage where intense, rapid feedback from a large number of WN stars briefly imprints nonuniform elemental enrichment patterns (i.e., elevated N/O), which are expected to be quickly washed away. As soon as the system evolves beyond the WN phase, subsequent WC or CCSN yields will rapidly dilute the N excess and alter the overall abundance patter (e.g., increasing C/O, lowering N/C).

Recently, M. W. Topping et al. (2025b) showed that galaxies with significant N IV] emission (corresponding to extreme N/O enhancement), are found exclusively among galaxies with extreme [O III]+Hβ EWs of 2600–4200 Å. Galaxies with such high [O III]+Hβ EWs are in the upper 2% tail of the EW distribution at $z \gtrsim 4$ and are outliers at $z \sim 0$. This strongly suggests that high N/O outliers are confined to the youngest stellar populations undergoing their most intense bursts of star formation in the early Universe (e.g., R. Endsley et al. 2023, 2025; J. Matthee et al. 2023; M. W. Topping et al. 2025b).

In this context, M. W. Topping et al. (2025b) found that 30% of galaxies with EW[O III] + Hβ > 2000 Å show strong nitrogen emission, corresponding to ∼0.6% of their UV-selected parent population. If this 0.6% population corresponds to enhanced N/O during the $\Delta t_{\rm WN} \sim 0.3$ Myr WN phase, it would imply a characteristic burst timescale of ∼50 Myr. A practical consequence is that young bursts substantially increase the light-to-mass ratios and, thus, the likelihood of detection in flux-limited samples (e.g., C. A. Mason et al. 2023; J. B. Muñoz et al. 2023; G. Sun et al. 2023). Therefore, the observed frequency of strong nitrogen emitters at fixed $M_{\rm UV}$ is likely biased high relative to their intrinsic abundance (e.g., at fixed stellar mass). Given the detectability bias toward burst phases, this $t_{\rm burst}$ may represent a lower limit, with the true interval plausibly longer. This timescale is supported by recent analyses of the scatter in the star-forming main sequence and time-resolved SFR indicators at $z \sim 3$–9 that suggest burst cycles of tens-of-megayear timescales (albeit with broad distributions, e.g., C. Simmonds et al. 2025). Thus, the combination of extreme-EW selection and N IV] frequency provides a novel timing argument that WN-driven enrichment is tightly coupled to very young, transient starburst phases beyond cosmic noon.

Taken together, the arguments presented in this work suggest that nitrogen outliers are not exotic exceptions, but rather a brief, WN-enriched phase that any high-redshift galaxy with sufficiently high SFR surface density can pass through. In contrast, numerous low-redshift WR galaxies exhibit young populations that include WN and WC stars but show little or no N/O enhancement (e.g., Y. I. Izotov et al. 2006; C. Kehrig et al. 2013). This difference underscores that similar stellar populations do not guarantee the same chemical signatures; instead, the extreme densities, compactness, and rapid mixing timescales of high-redshift starbursts likely make WN-driven enrichment both more pronounced and more transient. In this view, N/O outliers in the early Universe are not anomalies, but rather are the chemical fingerprints of galaxies caught midburst, showing fleeting yet inevitable markers of early galaxy evolution.

6. Conclusions

We have presented a detailed enrichment scenario by WN stars that explains the extreme nitrogen enrichment in the metal-poor (∼10% $Z_\odot$), high surface-density ($1.34 \times 10^3\,M_\odot$ pc^{-2}), high-redshift ($z = 6.1025$), lensed galaxy RXCJ2248-ID3. These measurements were made possible by exceptionally deep JWST/NIRSpec medium-resolution spectroscopy of RXCJ2248-ID3, obtained as part of the GLIMPSE-D survey. The unprecedented depth and S/N of the GLIMPSE-D spectrum allow spectral measurements typically limited to the nearby Universe, including consistent broad components in the Balmer series and [O III] λ4364 and $\lambda\lambda$4960,5008 lines, faint [Ar IV] $\lambda\lambda$4713,4741 emission, and signatures of WR stars. Specifically, we detected the emission characteristic of WN-type stars, including strong N III λ4642 and broadened He II λ1640 and λ4687 emission, marking RXCJ2248-ID3 as the most distant galaxy to date with spectroscopic detections of WR stars.

We performed a detailed nebular analysis, self-consistently measuring the reddening, high-ionization temperature (T_e(O^{+2})), and densities from five different diagnostics across a wide ionization range. We measure a low reddening value of $E(B-V) = 0.052^{+0.110}_{-0.052}$ from the Hγ/Hβ ratio but find an excess in the Hα/Hβ ratio of 0.204 due to collisional excitation of Hα. The measured densities span the range of $1.15 \times 10^3\,{\rm cm}^{-3} \leqslant n_e \leqslant 2.65 \times 10^5\,{\rm cm}^{-3}$ and show strong evidence for nebular density stratification, with systematically higher densities in the highest-ionization gas and UV emission tracing gas at higher densities than those traced by optical diagnostics. This structure implies a highly clumpy, multiphase ISM. We note that such high-density, multiphase gas leads to densities from optical diagnostics that are biased to the low end of the density range due to their low critical densities. Therefore, we recommend using UV density diagnostics because they are more robust in high-density environments: n_e(Si^{+2}), n_e(C^{+2}), and n_e(N^{+3}) trace the densities in the low-, intermediate-, and high-ionization gas, respectively. As a result, we measure a direct-method metallicity of $12 + \log(\mathrm{O/H}) = 7.753 \pm 0.025$.

Using the full rest-UV+optical spectra, we present the first robust, consistent measurements of N/O abundance in any galaxy using three ionization stages of nitrogen ($\mathrm{N}^{+}/\mathrm{O}^{+}$, $\mathrm{N}^{+2}/\mathrm{O}^{+2}$, $\mathrm{N}^{+3}/\mathrm{O}^{+2}$). The uniformity of our N/O measurements suggests that the N/O enrichment is spatially extended and well mixed throughout the ionized ISM. Empirical trends suggest C/O should follow a similar trend as N/O, and thus also be enhanced. In contrast, we find C/O to be significantly depleted relative to N/O, suggesting nonuniform elemental enrichment likely driven by WN stars with little to no contribution from WC stars.

The CNO abundance pattern is best reproduced by a modified version of the dual-burst chemical evolution model from C. Kobayashi & A. Ferrara (2024) that reduces the contribution from WC stars relative to WN stars, as expected in metal-poor environments. The resulting short-lived WN phase ejects N-rich, C-poor material. We use this chemical evolution model to assess whether the observed N mass can plausibly arise from the recent star formation in RXCJ2248-ID3 and estimate an ionized N mass of 435 $M_{\odot}$. This value is consistent with the N mass estimated from the observed emission lines of $18.2 - 57.5\,M_{\odot}$ if $4 - 13\%$ of the N gas is ionized.

These results demonstrate that standard stellar evolution models can reproduce both the CNO pattern and the total nitrogen mass observed without invoking an exotic IMF or enrichment channel. The uniform N/O ratios across multiple ionization zones further suggest that the WN yields were rapidly mixed into a relatively pristine ambient ISM, preserving the global enhancement observed in RXCJ2248-ID3. Although RXCJ2248-ID3 exhibits strong density and temperature stratification, this structural complexity does not necessarily imply chemical inhomogeneity. The consistent N/O ratios across ions tracing vastly different physical conditions indicate that the enriched material was efficiently dispersed throughout the multiphase ISM. In such a compact ($R_e \approx 20$ pc), high-pressure environment, turbulent and radiative mixing can homogenize the chemical composition on timescales comparable to, or shorter than, the brief WN phase itself, yielding a chemically uniform yet physically clumpy nebula.

Importantly, the abundance pattern and physical conditions observed in RXCJ2248-ID3 can only be explained if the galaxy is caught during a narrow evolutionary window within a few megayears of a massive, compact starburst when WN stars dominate chemical feedback. At low metallicity, stars require higher initial masses to reach the WR phase, making such enrichment episodes rare and dependent on sufficiently high SFRs to fully populate the upper IMF. Furthermore, the WN phase itself is extremely short-lived (~0.03–0.3 Myr) and easily masked by subsequent WC winds, CCSNe, or AGB stars contributions. These timing and SFR constraints make WR-driven N/O enhancement a rare phenomenon associated with extreme starburst conditions that are more common in the early Universe, and which are scarce in the local Universe.

Our results suggest that the WN-driven N/O enrichment we observe is not a peculiar property of a single system, but rather a brief phase that essentially all high-redshift galaxies ($z > 5$) with sufficiently high SFR surface densities to produce significant numbers of WN stars likely undergo. In particular, the work of M. W. Topping et al. (2025b) can be used to link N/O outliers to the most extreme [O III]+Hβ EWs. The observed frequency of such EWs combined with the short lifetime of the WN phase implies a burst cycle of order ~50 Myr, consistent with galaxies repeatedly cycling through short, bursty episodes of enrichment. Thus, the GLIMPSE-D spectrum of RXCJ2248-ID3 provides not only the first direct evidence of WN stars shaping the chemical evolution of $z > 5$ galaxies but also a timing argument that situates N/O outliers as a natural, fleeting, phase of high-redshift star formation.

Taken together, our findings are a glimpse into a short-lived phase of chemically selective enrichment from WN stars at cosmic dawn, providing a physically self-consistent solution to the extreme N/O enhancement and relative C/O depletion observed in RXCJ2248-ID3 and galaxies like it. Thus, RXCJ2248-ID3 serves as a benchmark case for interpreting chemically enriched, stratified, multiphase starbursts in the early Universe.

Acknowledgments

We thank the referee for their thorough review of our calculations and analysis and for their helpful suggestions, which greatly improved the robustness of our results and the clarity of the text. This work is based on observations made with the NASA/ESA/CSA James Webb Space Telescope. The data were obtained from the Mikulski Archive for Space Telescopes at the Space Telescope Science Institute, which is operated by the Association of Universities for Research in Astronomy, Inc., under NASA contract NAS 5-03127 for JWST. These observations are associated with program #9223. This work has received funding from the Swiss State Secretariat for Education, Research and Innovation (SERI) under contract No. MB22.00072, as well as from the Swiss National Science Foundation (SNSF) through project grant 200020_207349. The Cosmic Dawn Center (DAWN) is funded by the Danish National Research Foundation under grant DNRF140. The Dunlap Institute is funded through an endowment established by the David Dunlap family and the University of Toronto. We acknowledge the support of the Canadian Space Agency (CSA) [25JWGO4A06]. HA acknowledges support from CNES, focused on the JWST mission, and the Programme National Cosmology and Galaxies (PNCG) of CNRS/INSU with INP and IN2P3, co-funded by CEA and CNES and support by the French National Research Agency (ANR) under grant ANR-21-CE31-0838. The JWST data presented in this article from program #9223 were obtained from the Mikulski Archive for Space Telescopes (MAST) at the Space Telescope Science Institute. The specific observations analyzed can be accessed via DOI: 10.17909/8642-1k68.

Facility: JWST (NIRSpec).

Software: `astropy` (The Astropy Collaboration et al. 2013, 2018, 2022), `calwebb`, `jupyter` (T. Kluyver et al. 2016), `numpy` version 1.26 (C. R. Harris et al. 2020), `PyNeb` version 1.1.14 (V. Luridiana et al. 2015), `python`, `lmfit` (M. Newville et al. 2015), `mpfit` (C. B. Markwardt 2009), `scipy.optimize.curve_fit`, `BAGPIPES` (A. C. Carnall et al. 2018), `BPASS` version 2.14 (J. J. Eldridge et al. 2017), `cloudy` version 23.01 (M. Chatzikos et al. 2023; C. M. Gunasekera et al. 2023), `msaexp` pipeline version 0.9.8 (G. Brammer 2022).

ORCID iDs

Danielle A. Berg https://orcid.org/0000-0002-4153-053X
Rohan P. Naidu https://orcid.org/0000-0003-3997-5705
John Chisholm https://orcid.org/0000-0002-0302-2577
Hakim Atek https://orcid.org/0000-0002-7570-0824
Seiji Fujimoto https://orcid.org/0000-0001-7201-5066
Vasily Kokorev https://orcid.org/0000-0002-5588-9156
Lukas J. Furtak https://orcid.org/0000-0001-6278-032X
Chiaki Kobayashi https://orcid.org/0000-0002-4343-0487
Daniel Schaerer https://orcid.org/0000-0001-7144-7182
Angela Adamo https://orcid.org/0000-0002-8192-8091
Qinyue Fei https://orcid.org/0000-0001-7232-5355
Damien Korber https://orcid.org/0000-0002-3897-6856
Jorryt Matthee https://orcid.org/0000-0003-2871-127X
Rui Marques-Chaves https://orcid.org/0000-0001-8442-1846
Zorayda Martinez https://orcid.org/0009-0000-2997-7630
Kristen. B. W. McQuinn https://orcid.org/0000-0001-5538-2614
Julian B. Muñoz https://orcid.org/0000-0002-8984-0465
Pascal A. Oesch https://orcid.org/0000-0001-5851-6649
Alberto Saldana-Lopez https://orcid.org/0000-0001-8419-3062
Daniel P. Stark https://orcid.org/0000-0001-6106-5172
Mabel G. Stephenson https://orcid.org/0000-0003-4717-0376
Tiger Yu-Yang Hsiao https://orcid.org/0000-0003-4512-8705

References

Abdurro'uf, Larson, R. L., Coe, D., et al. 2024, ApJ, 973, 47

Aguilera-Dena, D. R., Langer, N., Antoniadis, J., et al. 2022, A&A, 661, A60

Arellano-Córdova, K. Z., Berg, D. A., Mingozzi, M., et al. 2025, MNRAS, 544, 1588

Asplund, M., Amarsi, A. M., & Grevesse, N. 2021, A&A, 653, A141

Atek, H., Chisholm, J., Kokorev, V., et al. 2026, arXiv:2511.07542

Balestra, I., Vanzella, E., Rosati, P., et al. 2013, A&A, 559, L9

Berg, D. A., Chisholm, J., Erb, D. K., et al. 2021, ApJ, 922, 170

Berg, D. A., Erb, D. K., Auger, M. W., Pettini, M., & Brammer, G. B. 2018, ApJ, 859, 164

Berg, D. A., Erb, D. K., Henry, R. B. C., Skillman, E. D., & McQuinn, K. B. W. 2019, ApJ, 874, 93

Berg, D. A., James, B. L., King, T., et al. 2022, ApJS, 261, 31

Berg, D. A., Pogge, R. W., Skillman, E. D., et al. 2020, ApJ, 893, 96

Berg, D. A., Skillman, E. D., Chisholm, J., et al. 2024, ApJ, 971, 87

Berg, D. A., Skillman, E. D., Henry, R. B. C., Erb, D. K., & Carigi, L. 2016, ApJ, 827, 126

Berg, D. A., Skillman, E. D., Marble, A., et al. 2012, ApJ, 754, 98

Boco, L., Mapelli, M., Sander, A. A. C., et al. 2025, A&A, 703, A243

Boone, F., Clément, B., Richard, J., et al. 2013, A&A, 559, L1

Brammer, G. 2022, msaexp: NIRSpec Analyis Tools, v0.3, Zenodo, doi:10.5281/zenodo.7299500

Brinchmann, J., Kunth, D., & Durret, F. 2008, A&A, 485, 657

Bunker, A. J., Saxena, A., Cameron, A. J., et al. 2023, A&A, 677, A88

Burke, C. J., Liu, X., Chen, Y.-C., Shen, Y., & Guo, H. 2021, MNRAS, 504, 543

Calzetti, D., Armus, L., Bohlin, R. C., et al. 2000, ApJ, 533, 682

Cameron, A. J., Katz, H., Rey, M. P., & Saxena, A. 2023, MNRAS, 523, 3516

Cardelli, J. A., Clayton, G. C., & Mathis, J. S. 1989, ApJ, 345, 245

Carnall, A. C., McLure, R. J., Dunlop, J. S., & Davé, R. 2018, MNRAS, 480, 4379

Castellano, M., Napolitano, L., Fontana, A., et al. 2024, ApJ, 972, 143

Cataldi, E., Belfiore, F., Curti, M., et al. 2025, A&A, 703, A208

Charbonnel, C., Schaerer, D., Prantzos, N., et al. 2023, A&A, 673, L7

Chatzikos, M., Bianchi, S., Camilloni, F., et al. 2023, RMxAA, 59, 327

Chiappini, C., Romano, D., & Matteucci, F. 2003, MNRAS, 339, 63

Choustikov, N., Katz, H., Cameron, A. J., et al. 2025, OJAp, 9

Claeyssens, A., Adamo, A., Kokorev, V., et al. 2026, arXiv:2601.16281

Claeyssens, A., Adamo, A., Messa, M., et al. 2025, MNRAS, 537, 2535

Crespo Gómez, A., Tamura, Y., Colina, L., et al. 2026, arXiv:2511.14658

Crowther, P. A. 2007, ARA&A, 45, 177

Curti, M., Cataldi, E., Belfiore, F., et al. 2025b, arXiv:2509.06622

Curti, M., Witstok, J., Jakobsen, P., et al. 2025a, A&A, 697, A89

de Graaff, A., Brammer, G., Weibel, A., et al. 2025, A&A, 697, A189

de Graaff, A., Rix, H.-W., Carniani, S., et al. 2024, A&A, 684, A87

Eldridge, J. J., Stanway, E. R., Xiao, L., McClelland, L. A. S., et al. 2017, PASA, 34, e058

Endsley, R., Chisholm, J., Stark, D. P., Topping, M. W., & Whitler, L. 2025, ApJ, 987, 189

Endsley, R., Stark, D. P., Whitler, L., et al. 2023, MNRAS, 524, 2312

Esteban, C., Bresolin, F., Peimbert, M., et al. 2009, ApJ, 700, 654

Esteban, C., García-Rojas, J., Carigi, L., et al. 2014, MNRAS, 443, 624

Esteban, C., Peimbert, M., Torres-Peimbert, S., & Rodríguez, M. 2002, ApJ, 581, 241

Fujimoto, S., Naidu, R. P., Chisholm, J., et al. 2025, ApJ, 989, 46

Furtak, L., Zitrin, A., Zackrisson, E., et al. 2026, arXiv:2604.18696

Galliano, F., Galametz, M., & Jones, A. P. 2018, ARA&A, 56, 673

García-Rojas, J., & Esteban, C. 2007, ApJ, 670, 457

Garnett, D. R. 1990, ApJ, 363, 142

Garnett, D. R. 1992, AJ, 103, 1330

Garnett, D. R., Dufour, R. J., Peimbert, M., et al. 1995, ApJL, 449, L77

Garnett, D. R., Shields, G. A., Peimbert, M., et al. 1999, ApJ, 513, 168

Götberg, Y., de Mink, S. E., Groh, J. H., Leitherer, C., & Norman, C. 2019, A&A, 629, A134

Gräfener, G., Owocki, S. P., Grassitelli, L., & Langer, N. 2017, A&A, 608, A34

Gräfener, G., & Vink, J. S. 2015, A&A, 578, L2

Gunasekera, C. M., van Hoof, P. A. M., Chatzikos, M., & Ferland, G. J. 2023, RNAAS, 7, 246

Gunawardhana, M. L. P., Brinchmann, J., Croom, S., et al. 2025, MNRAS, 543, 3172

Harikane, Y., Inoue, A. K., Ellis, R. S., et al. 2025a, ApJ, 980, 138

Harikane, Y., Sanders, R. L., Ellis, R., et al. 2025b, ApJ, 993, 204

Harris, C. R., Millman, K. J., van der Walt, S. J., et al. 2020, Natur, 585, 357

Hayes, M. J., Saldana-Lopez, A., Citro, A., et al. 2025, ApJ, 982, 14

Heintz, K. E., Brammer, G. B., Watson, D., et al. 2025, A&A, 693, A60

Heintz, K. E., Watson, D., Brammer, G., Vejlgaard, S., et al. 2024, Sci, 384, 890

Henry, R. B. C., Edmunds, M. G., & Köppen, J. 2000, ApJ, 541, 660

Hsiao, T. Y.-Y., Topping, M. W., Coe, D., et al. 2025, ApJ, 993, 70

Isobe, Y., Maiolino, R., Ji, X., et al. 2026, MNRAS, 547, stag123

Isobe, Y., Ouchi, M., Nakajima, K., et al. 2023, ApJ, 956, 139

Izotov, Y. I., Schaerer, D., Blecha, A., et al. 2006, A&A, 459, 71

Izotov, Y. I., & Thuan, T. X. 1999, ApJ, 511, 639

Izotov, Y. I., & Thuan, T. X. 2007, ApJ, 665, 1115

Izotov, Y. I., & Thuan, T. X. 2008, ApJ, 687, 133

James, B. L., Auger, M., Aloisi, A., Calzetti, D., & Kewley, L. 2016, ApJ, 816, 40

James, B. L., Berg, D. A., King, T., et al. 2022, ApJS, 262, 26

Ji, X., Belokurov, V., Maiolino, R., et al. 2026, MNRAS, 545, staf2110

Ji, X., Übler, H., Maiolino, R., et al. 2024, MNRAS, 535, 881

Katz, H., Saxena, A., Cameron, A. J., et al. 2023, MNRAS, 518, 592

Kehrig, C., Pérez-Montero, E., Vílchez, J. M., et al. 2013, MNRAS, 432, 2731

Kennicutt, R. C., Jr. 1984, ApJ, 287, 116

Kennicutt, R. C., Jr. 1992, ApJ, 388, 310

Kluyver, T., Ragan-Kelley, B., Pérez, F., et al. 2016, in Positioning and Power in Academic Publishing: Players, Agents and Agendas, ed. F. Lozides & B. Schmidt (IOS Press), 87

Kobayashi, C., & Ferrara, A. 2024, ApJL, 962, L6

Kobayashi, C., Karakas, A. I., & Lugaro, M. 2020, ApJ, 900, 179

Kobayashi, C., Umeda, H., Nomoto, K., Tominaga, N., & Ohkubo, T. 2006, ApJ, 653, 1145

Kramarenko, I. G., Rosdahl, J., Blaizot, J., et al. 2026, A&A, 707, a184

Larson, R. L., Finkelstein, S. L., & Kocevski, D. D.a. 2023, ApJL, 953, L29

Limongi, M., & Chieffi, A. 2018, ApJS, 237, 13

López-Sánchez, Á. R., Esteban, C., García-Rojas, J., Peimbert, M., & Rodríguez, M. 2007, ApJ, 656, 168

Luridiana, V., Morisset, C., & Shaw, R. A. 2015, A&A, 573, A42

Mainali, R., Kollmeier, J. A., Stark, D. P., et al. 2017, ApJL, 836, L14

Maiolino, R., & Mannucci, F. 2019, A&ARv, 27, 3

Maiolino, R., Scholtz, J., Witstok, J., Carniani, S., et al. 2024, Natur, 627, 59

Markwardt, C. B. 2009, ASPC, 411251

Marques-Chaves, R., Schaerer, D., Kuruvanthodi, A., et al. 2024, A&A, 681, A30

Martinez, Z., Berg, D. B., James, B. L., et al. 2025, ApJ, 995, 36

Martins, F., Palacios, A., Schaerer, D., & Marques-Chaves, R. 2025, A&A, 698, A262

Martins, F., Schaerer, D., Marques-Chaves, R., & Upadhyaya, A. 2023, A&A, 678, A159

Mason, C. A., Trenti, M., & Treu, T. 2023, MNRAS, 521, 497

Massey, P., Neugent, K. F., & Levesque, E. M. 2017, RSPTA, 375, 20160267

Massey, P., Neugent, K. F., & Morrell, N. 2015, ApJ, 807, 81

Matthee, J., Mackenzie, R., Simcoe, R. A., et al. 2023, ApJ, 950, 67

Messa, M., Vanzella, E., Loiacono, F., et al. 2026, A&A, 705, A173

Meynet, G., & Maeder, A. 2005, A&A, 429, 581

Mingozzi, M., James, B. L., Berg, D. A., et al. 2022, ApJ, 939, 39

Monna, A., Seitz, S., Greisel, N., et al. 2014, MNRAS, 438, 1417

Muñoz, J. B., Mirocha, J., Furlanetto, S., & Sabti, N. 2023, MNRAS, 526, L47

Nagele, C., & Umeda, H. 2023, ApJL, 949, L16

Naidu, R. P., Oesch, P. A., Brammer, G., et al. 2026, OJAp, 9

Napolitano, L., Castellano, M., Pentericci, L., et al. 2025, ApJ, 989, 75

Neugent, K., & Massey, P. 2019, Galax, 7, 74

Neugent, K. F., & Massey, P. 2023, AJ, 166, 68

Newville, M., Stensitzki, T., Allen, D. B., & Ingargiola, A. 2015, LMFIT: Non-Linear Least-Square Minimization and Curve-Fitting for Python, v0.8.0, Zenodo, doi: 10.5281/zenodo.11813

Nicholls, D. C., Sutherland, R. S., Dopita, M. A., Kewley, L. J., & Groves, B. A. 2017, MNRAS, 466, 4403

Pascale, M., Dai, L., McKee, C. F., & Tsang, B. T. H. 2023, ApJ, 957, 77

Peña-Guerrero, M. A., Leitherer, C., de Mink, S., Wofford, A., & Kewley, L. 2017, ApJ, 847, 107

Pérez-Montero, E., Amorín, R., Sánchez Almeida, J., et al. 2021, MNRAS, 504, 1237

Pérez-Montero, E., & Contini, T. 2009, MNRAS, 398, 949

Pilyugin, L. S., & Thuan, T. X. 2005, ApJ, 631, 231

Rémy-Ruyer, A., Madden, S. C., Galliano, F., et al. 2014, A&A, 563, A31

Rivera-Thorsen, T. E., Chisholm, J., Welch, B., et al. 2024, A&A, 690, A269

Rogers, N. S. J., Skillman, E. D., Pogge, R. W., et al. 2022, ApJ, 939, 44

Roman-Duval, J., Jenkins, E. B., Tchernyshyov, K., et al. 2022, ApJ, 928, 90

Roy, J.-R., & Kunth, D. 1995, A&A, 294, 432

Sander, A. A. C., Lefever, R. R., Josiek, J., et al. 2026, NatAs, 10, 290

Sander, A. A. C., Vink, J. S., & Hamann, W. R. 2020, MNRAS, 491, 4406

Schaerer, D., Marques-Chaves, R., Xiao, M., & Korber, D. 2024, A&A, 687, L11

Schmidt, K. B., Huang, K.-H., Treu, T., et al. 2017, ApJ, 839, 17

Senchyna, P., Plat, A., Stark, D. P., & Rudie, G. C. 2024, ApJ, 966, 92

Senchyna, P., Stark, D. P., Vidal-García, A., et al. 2017, MNRAS, 472, 2608

Shi, Y., Dai, L., Murray, N., et al. 2026, ApJ, 997, 309

Shirazi, M., & Brinchmann, J. 2012, MNRAS, 421, 1043

Simmonds, C., Tacchella, S., McClymont, W., et al. 2025, MNRAS, 544, 4551

Stark, D. P., Topping, M. W., Endsley, R., & Tang, M. 2025, in Encyclopedia of Astrophysics, ed. J. Andrews et al., 4 (Elsevier), 453

Stasińska, G., & Schaerer, D. 1997, A&A, 322, 615

Sun, G., Faucher-Giguère, C.-A., Hayward, C. C., et al. 2023, ApJL, 955, L35

Tacchella, S., Eisenstein, D. J., Hainline, K., et al. 2023, ApJ, 952, 74

The Astropy Collaboration, Price-Whelan, A. M., Lim, P. L., et al. 2022, ApJ, 935, 167

The Astropy Collaboration, Price-Whelan, A. M., Sipőcz, B. M., et al. 2018, AJ, 156, 123

The Astropy Collaboration, Robitaille, T. P., Tollerud, E. J., et al. 2013, A&A, 558, A33

Topping, M. W., Sanders, R. L., Shapley, A. E., et al. 2025a, MNRAS, 541, 1707

Topping, M. W., Stark, D. P., Senchyna, P., et al. 2024, MNRAS, 529, 3301

Topping, M. W., Stark, D. P., Senchyna, P., et al. 2025b, ApJ, 980, 225

Tosi, M. 1988, A&A, 197, 33

Übler, H., Maiolino, R., Curtis-Lake, E., et al. 2023, A&A, 677, A145

Usui, M., Mawatari, K., Álvarez-Márquez, J., et al. 2025, ApJL, 991, L38

Valentino, F., Heintz, K. E., Brammer, G., et al. 2025, A&A, 699, A358

van Zee, L., & Haynes, M. 2006, ApJ, 636, 214

Vanzella, E., Grazian, A., Hayes, M., et al. 2010, A&A, 513, A20

Vincenzo, F., Miglio, A., Kobayashi, C., Mackereth, J. T., & Montalban, J. 2019, A&A, 630, A125

Vink, J. S. 2023, A&A, 679, L9

Watanabe, K., Ouchi, M., & Nakajima, K. o. 2024, ApJ, 962, 50